INTERNATIONAL JOURNAL FOR NUMERICAL METHODS IN FLUIDS

Int. J. Numer. Meth. Fluids 0000; **00**:2–37

Published online in Wiley InterScience (www.interscience.wiley.com). DOI: 10.1002/fld

Anisotropic Goal-oriented error analysis for a third-order accurate CENO Euler discretization

A. Carabias[1], A. Belme[2], A. Loseille[3], A. Dervieux[1*]

[1] *Université Côte d'Azur, INRIA Sophia Antipolis, 2004 route de Lucioles, 06902 Sophia-Antipolis, France, and Lemma, 2000 route des lucioles, 06410 Biot, France*

[2] *Université Pierre et Marie Curie, Institut Jean le Rond d'Alembert, Case 162, 4 Place Jussieu, 75252 Paris, France*

[3] *Inria Saclay Ile-de-France , Projet Gamma3, 1 rue Honoré d'Estienne d'Orves, 91126 Palaiseau, France.*

SUMMARY

In this paper a central-ENO approximation based on a quadratic polynomial reconstruction is considered for solving the unsteady 2D Euler equations. The scheme is third-order accurate on irregular unstructured meshes. The paper concentrates on a method for a metric-based goal-oriented mesh adaptation. For this purpose, an *a priori* error analysis for this CENO scheme is proposed. It allows us to get an estimate depending on the polynomial reconstruction error. As a third-order error is not naturally expressed in terms of a metric, we propose a least-square method to approach a third-order error by a quadratic term. Then an optimization problem for the best mesh metric is obtained and analytically solved. The resulting mesh optimality system is discretised and solved using a global unsteady fixed point algorithm. The method is applied to an acoustic propagation benchmark.

Keywords: Compressible flow, Hyperbolic, Euler flow, Finite volume, Error estimation, Mesh adaptation.

Received . . .

Copyright © 0000 John Wiley & Sons, Ltd.

Prepared using fldauth.cls *[Version: 2010/05/13 v2.00]*

1. INTRODUCTION

High-order approximations in Computational Mechanics are an attracting mean for obtaining computations with smaller approximation errors, or, more importantly in applications, for obtaining computations with less computer time and memory cost, thanks to the use of coarser meshes. However high-order approximations do not reduce mesh fineness constraints related to the size and number of details (e.g. monotony changes, stiff variations) in the different solution fields. Solely considering the asymptotic accuracy order may not be a sufficient quality criterion. An important example is the unsteady advection of waves in a gas, which will help us to list in more details some necessary qualities of a numerical scheme. We can distinguish five quality criteria. (i) Asymptotical convergence order α applies to smooth fields when mesh is *sufficiently fine*. Typically, for a space-time dimension of $dim + 1$, dividing all discretization sizes by two, will results in a computational cost roughly 2^{dim+1} times higher for an error divided by 2^{α}. The central issue in 2D or 3D is in the above "sufficiently fine" condition. (ii) Advective characteristics, dissipation and dispersion, are analysed on a Cartesian mesh. Their optimization should in some cases be prefered to best asymptotic convergence, see for example [53]. (iii) Accuracy on non-asymptotically fine meshes is difficult to analyse, but it is a paramount practical criterion. Typically, the user needs a good prediction with 6 to 12 mesh sizes for a wavelength. (iv) Accuracy on non-regular and non-structured meshes is also important. Asymptotic convergence can be evaluated by analysis and, more or less (what is a generic irregular mesh?), by numerical experiments. (v) We should also mention accuracy on singular solutions (or data), preferably avoiding spurious oscillations. But this issue is not addressed in this paper.

When considering Cartesian meshes, criterion (iv) can be discarded. But using Cartesian meshes may lead to use prohibitively fines meshes in presence of small scales or when singularities are encountered.

*Correspondence to: INRIA Sophia Antipolis, 2004 route de Lucioles, 06902 Sophia-Antipolis, France, alain.dervieux@inria.fr

Prepared using fldauth.cls
DOI: 10.1002/fld

Another option is to apply mesh adaptive strategies. In the case of isotropic mesh adaptation, the $h-p$ methods which control together mesh local size and scheme local accuracy have shown an impressive efficiency in addressing mechanical problems involving many details and scales, see for example [51]. When the fields under study involve structures of lower dimension, like quasi-planar waves or discontinuity curves in 2D, an anisotropic mesh adaptation may be necessary. Anisotropic Hessian-based error estimates, combined with a metric for representing the mesh, showed efficiency for linear (second-order accurate) finite-element-type approximations, cf. [9, 14, 25, 29, 31, 33, 39, 49, 52, 54]. The association between metrics and linear elements is rather naturally derived since the optimal metric is a scalar factor times the numerically recovered Hessian of the variable chosen as sensor.

Then the extension to third-order accuracy appears as the next step. Examining the P_2-interpolation error on a sensor leads to consider the trilinear third-order term of its Taylor series. It is possible to imagine a mesh adaptation which is controlled directly by these third-order derivatives. See for example [7, 17]. In the present paper we shall less ambitiously propose to convert the trilinear information of the error estimate into a bilinear one, namely a pseudo-Hessian-based error model globally scaled to the required order.

Mesh adaptation based on the interpolation error of one or several unknowns takes into account very incompletely the approximation error. A more accurate issue is to address the reduction of the approximation error committed on a scalar output. Initially restricted to interpolation errors, anisotropic error estimates are now available for goal-oriented formulations, see [4, 28, 37, 41, 10]. In particular, *a priori* estimates have become an efficient tool for addressing mesh adaptation issues for steady Euler flows [41], then for unsteady Euler flows [13], and more recently for steady and unsteady Navier-Stokes ones [11]. In these works, the error analysis follows the so-called *a priori* implicit error method, dealing with a discrete invertible system for the deviation between discrete solution and a projection of the continuous one. Such *a priori* estimates were obtained for a second-order mixed-element-volume approximation close to the usual $\mathcal{P}^1$ finite element. Promises given by theory were kept by numerical demonstrators, showing second-order convergence for

Prepared using fldauth.cls
DOI: 10.1002/fld

shocked flows, [43]. The theory also predicts higher-order convergence for the higher-order interpolation of singular flows. A necessary condition is the application of an anisotropic strategy, involving an anisotropic error estimate.

In this paper we consider the appication of a third-order accurate Central Essentially Non-Oscillatory central (CENO) approximation, based on a quadratic polynomial reconstruction, for approximating the Euler equations. It is inspired by the CENO proposition of Groth and coworkers, see [36]. We prealably transpose it to a vertex formulation. Because the third-order upwind scheme is rather dissipative, a transformation is proposed in order to improve the approximation properties of the scheme according to the above criteria, focusing on its advective performances. As for the original unstructured CENO scheme [21], the new scheme is third-order accurate on irregular unstructured meshes.

We examine (Sec.2) how to evaluate reconstruction errors. We present (Sec.3) shortly the numerical scheme which has been designed for our investigation. We develop in Sec.4 an error estimate based on the PDE, in order to build a goal-oriented mesh adaptation algorithm. The resulting *a priori* error analysis is a kind of dual of the *a posteriori* analysis of Barth and Larson [7]. Sec.5 considers the extension of a metric-based adaptation method to take into account the cubic reconstruction error. In [17], Cao proposes a first approximation of this error with stretching directions. In the present paper, we propose to replace the application of the third derivative tensor to a mesh size vector by the power $3/2$ of the application of a pseudo-Hessian second-order tensor to this mesh size. The optimal metric is defined in Sec.6. Applications are considered in Sec.7. An unsteady model addressed. For solving the resulting mesh optimality system, we discretise it and apply the global unsteady fixed point algorithm of [12, 13] for unsteady flows. In Sec.8, the unsteady method is applied to an acoustic propagation benchmark and compared with previous approaches.

Prepared using fldauth.cls
DOI: 10.1002/fld

2. HIGHER ORDER INTERPOLATION AND RECONSTRUCTION

Most high-order approximation schemes like Discontinous Galerkin [8, 23, 24, 50], ENO [6, 26, 30, 38] or distributive schemes [2] use kth-order interpolation or reconstruction and are k-exact. Interpolation and reconstruction are two approximation mappings, the errors of which need to be analysed. Most analyses are inspired by the Bramble-Hilbert principle, saying that an approximation which is exact for kth-order polynomial is a $(k+1)$th-order accurate approximation. Demonstrations can be found in the fundamental paper [22]. Later, when considering reconstruction-based schemes, see [27], the authors refered to the Taylor series. A re-visitation in [1] establishes the link with [22]. Interpolation errors are used for building adaptation criteria in [34]. Several metrics are derived from the Hessians of each partial derivative. Then the metrics are intersected. A similar idea is in [32]. Intersections of metrics do not produce really optimal meshes. Further they often result in loosing anisotropy. A true asymptotic extension is proposed in [16],[18]. We also refer to [47] for similar ideas. A singular Sylvester decomposition is applied in [45].

Let us focus in this section on the estimation of the *reconstruction error*. Given a function sufficiently smooth u defined on a bounded domain Ω limited by a continuous boundary, given a tesselation of Ω into cells C_i of centroids $\mathbf{c}_i$, and the array $\bar{u} = \{\bar{u}_i\}$ of means of u on cells C_i, we are interested by polynomials $R_i(\mathbf{x}, \bar{u})$ of degree k built on any cell i and of same mean on cell i as u :

$$R_i(\mathbf{x}, \bar{u}) = \sum_{m=0}^{k} \frac{1}{m!} \sum_{|\ell|=m} (\mathbf{x} - \mathbf{c}_i)^\ell D_\ell, \quad \forall \mathbf{x} \in C_i, \quad \int_{C_j} R_i(\mathbf{x}, \bar{u}) dV = \bar{u}_j, \quad \forall\, j \in J(i)$$

where $J(i)$ a set of cells close to cell C_i and ℓ holds for the usual multi-index notation, in 2D:

$$\ell = (\alpha_1, \alpha_2), \quad ; \quad (\mathbf{x} - \mathbf{c}_i)^\ell = (x - c_i^x)^{\alpha_1} (y - c_i^y)^{\alpha_2} \quad ; \quad D_\ell = \frac{\partial^{\alpha_1}}{\partial x^{\alpha_1}} \frac{\partial^{\alpha_2}}{\partial y^{\alpha_2}}.$$

According to [27], for a sufficiently large neighborhood $J(i)$ of cells around i, we have :

$$D_\ell = \frac{\partial^\ell u}{\partial x_\ell}(\mathbf{c}_i) + O(h^{k+1-|\ell|}) \quad \text{and} \quad R_i(\mathbf{x}, \bar{u}) = u(\mathbf{x}) + O(h^{k+1}).$$

Prepared using fldauth.cls
DOI: 10.1002/fld

where diameters of cells are less than h. Note that if we define the operator:

$$\Pi : u \mapsto \Pi u, \quad \forall i,\ \forall \mathbf{x} \in C_i,\ \ \Pi u(\mathbf{x}) = R_i(\mathbf{x}, \bar{u})$$

then, as far as the $J(i)$'s are sufficiently large, Π is k-exact (mapping a kth-order polynomial in itself). In [1], the authors uses a result from [22] to give a more accurate estimate in the Sobolev space $W^{m,p}(\Omega)$ equipped of the following norm and semi-norm: $||.||_{m,p,\Omega}$:

$$||u||_{m,p,\Omega} = \left(\sum_{|\ell|=0}^{|\ell|=m} ||D^\ell u||_{p,\Omega}^p \right)^{\frac{1}{p}}, \quad |u|_{m,p,\Omega} = \left(\sum_{|\ell|=m} ||D^\ell u||_{p,\Omega}^p \right)^{\frac{1}{p}}.$$

It writes:

$$||u - \Pi u||_{m,p,\Omega} \ \leq \ C|u|_{k+1,p,\Omega} \ \frac{h^{k+1}}{\rho^m}$$

for a certain constant C, and where ρ is related to the shape of cells and m is any integer such that $0 \leq m \leq k+1$. This shows that the reconstruction error is, when $k = 2$, effectively expressed in terms of the third derivative of u.

A last remark is that in the case of a mean-square based reconstruction, if the number of cells of the support is exactly the number of unknown coefficients, then the minimum of the least-square functional is zero which shows (for a smooth function) that the reconstruction is equal to the initial function in one point of each neighboring cell, in other words, the reconstruction is an interpolation, the error of which is given by the Taylor expansion. In the general case, we do not have a precise estimate and we choose to get inspired by the Taylor expansion and heuristically write our reconstruction error estimate as follows:

$$||u - \Pi u(\mathbf{x})| \preceq \frac{1}{3!} \sup_{\delta\mathbf{x}} |D^3 u(\delta\mathbf{x})^3| \,.$$

where $\preceq$ holds for an inequality which holds for mesh size sufficiently small and where the $\delta\mathbf{x}$ describes the local mesh sizes in all the space directions.

Prepared using fldauth.cls
DOI: 10.1002/fld

3. CENO APPROXIMATION FOR THE 2D EULER EQUATIONS

3.1. Model

The unsteady 2D Euler equations in a geometrical bounded domain $\Omega \subset \mathbb{R}^2$ of boundary Γ can be written:

$$\text{Find } u \in \mathcal{V} \text{ such that } \int_0^T \int_\Omega \left(v\frac{\partial u}{\partial t} + v\nabla \cdot \mathcal{F}(u)\right) d\Omega\, dt = \int_0^T \int_\Gamma v\mathcal{F}_\Gamma(u)\, d\Gamma\, dt, \quad \forall\, v \in \mathcal{V}. \quad (1)$$

Here $\mathcal{V} = L^2\big(0,T;H^1(\Omega)\big) \cap H^1\big(0,T;L^2(\Omega)\big)$ and $u = (u_1, u_2, u_3, u_4)$ holds for the conserved unknowns (density, moments components, energy) and

$$\nabla \cdot \mathcal{F} = (\nabla \cdot \overline{\mathcal{F}_1}, \nabla \cdot \overline{\mathcal{F}_2}, \nabla \cdot \overline{\mathcal{F}_3}, \nabla \cdot \overline{\mathcal{F}_4}) \quad (2)$$

with

$$\mathcal{F} = (\overline{\mathcal{F}_1^x}, \overline{\mathcal{F}_1^y}, \overline{\mathcal{F}_2^x}, \overline{\mathcal{F}_2^y}, \overline{\mathcal{F}_3^x}, \overline{\mathcal{F}_3^y}, \overline{\mathcal{F}_4^x}, \overline{\mathcal{F}_4^y}) = (\mathcal{F}_1, ..., \mathcal{F}_8) \quad (3)$$

for the usual four Euler fluxes of mass, moments, energy. As right-hand side we have an integral of the various boundary fluxes $\mathcal{F}_\Gamma$ for various boundary conditions, which we do not need to detail here. Defining

$$B(u,v) = \int_0^T \int_\Omega \left(v\frac{\partial u}{\partial t} + v\nabla \cdot \mathcal{F}(u)\right) d\Omega\, dt - \int_0^T \int_\Gamma v\mathcal{F}_\Gamma(u)\, d\Gamma\, dt,$$

the variational formulation writes:

$$\text{Find } u \in \mathcal{V} \text{ such that } B(u,v) = 0, \quad \forall\, v \in \mathcal{V}. \quad (4)$$

3.2. CENO formulation

We choose a reconstruction-based finite-volume method, getting inspired by the unlimited version of the reconstruction technique of Barth [5] and of the CENO methods developed by Groth and co-workers, [35]. Concerning the location of the nodes with respect to the mesh elements, we prefer to minimize the number of unknowns with respect to a given mesh and therefore we keep the vertex-centered location already successfully used for second-order anisotropic (Hessian-based or

Prepared using fldauth.cls
DOI: 10.1002/fld

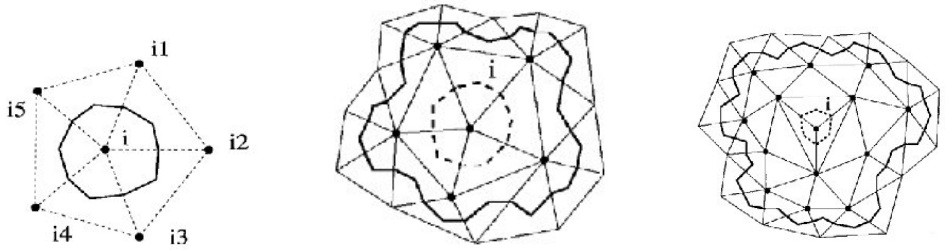

Figure 1. Dual cell and two reconstruction molecules

Goal-oriented) mesh adaptation [3, 13, 41]. For a more detailed description of the CENO approach presented here see [48]. Its main features are: (a) vertex centered, (b) dual median cells around the vertex, (c) a single mean square quadratic reconstruction for each dual cell (d) Roe approximate Riemann solver for stabilization, (e) explicit multi-stage time-stepping.

The computational domain is divided in triangles and in a dual tesselation in cells, each cell C_i being built around a vertex i, with limits following sections of triangle medians (Fig.1). We define the discrete space $\mathcal{V}_0$ of functions of $\mathcal{V}$ which are constant on any dual cell C_i. Let us define a *discrete reconstruction operator* R_2^0. The operator R_2^0 reconstructs a function of $\mathcal{V}_0$ in each cell C_i under the form of a second-order polynomial: $R_2^0 u_0|_{C_i} = \mathcal{P}_i^2(\mathbf{x})$. Given the means $(\overline{u_{0,i}}, i = 1, ...)$ of u_0 on cells C_i, $\mathcal{P}_i^2(\mathbf{x})$ is defined by the $c_{i,\alpha}$, $|\alpha| \leq k$ such that:

$$\mathcal{P}_i^2(\mathbf{x}) = \overline{u_{0,i}} + \sum_{|\alpha| \leq k} c_{i,\alpha}[(\mathbf{x}-\mathbf{c}_i)^\alpha - \overline{(\mathbf{x}-\mathbf{c}_i)^\alpha}]$$

$$\overline{\mathcal{P}_{i,i}} = \overline{u_{0,i}} \quad ; \quad (c_{i,\alpha}, |\alpha| \leq k) \;=\; Arg\min \sum_{j \in N(i)} (\overline{\mathcal{P}_{i,j}} - \overline{u_{0,j}})^2$$

where $\overline{\mathcal{P}_{i,j}}$ stands for the mean of $\mathcal{P}_i^2(\mathbf{x})$ on cell j, and the set of neighboring cells is taken sufficiently large for an accurate quadratic reconstruction (see Fig.1).

For the Euler model (4), the semi-discretized CENO scheme writes:

$$\text{Find } u_0 \in \mathcal{C}^1([0,T];\mathcal{V}_0) \text{ such that } B(R_2^0 u_0, v_0) \;=\; 0 \quad \forall\, v_0 \in \mathcal{C}^1([0,T];\mathcal{V}_0) \text{ with:}$$

$$B_h(R_2^0 u_0, v_0) \;=$$

$$\int_{\Omega\times[0,T]} v_0 \frac{\partial R_2^0 u_0}{\partial t}\, d\Omega \;+\; \int_{\Omega\times[0,T]} v_0 \nabla_h \cdot \mathcal{F}(R_2^0 u_0)\, d\Omega dt \;-\; \int_{\Gamma\times[0,T]} v_0 \mathcal{F}_\Gamma(R_2^0 u_0)\, d\Gamma\, dt \qquad (5)$$

Prepared using fldauth.cls
DOI: 10.1002/fld

In (5), the term $\nabla_h \cdot \mathcal{F}(R_2^0 u_0)$ needs to be defined, since $\mathcal{F}(R_2^0 u_0)$ is discontinuous at cells interfaces. Taking v_0 as a characteristic function of cell C_i, we get a finite volume formulation:

$$\forall C_i, \quad \int_{C_i} \frac{\partial R_2^0 u_0}{\partial t}\, d\Omega \;+\; \int_{C_i} \nabla_h \cdot \mathcal{F}(R_2^0 u_0)\, d\Omega \;-\; \int_{\partial C_i \cap \Gamma} \mathcal{F}_\Gamma(R_2^0 u_0)\, d\Gamma \;=\; 0 \quad \forall t.$$

or (using $\overline{\mathcal{P}_{i,i}} = \overline{u_{0,i}}$):

$$\forall C_i, \quad \frac{\partial}{\partial t} \int_{C_i} u_0\, d\Omega \;+\; \int_{\partial C_i} \mathcal{F}(R_2^0 u_0) \cdot \mathbf{n}\, d\Gamma - \int_{\partial C_i \cap \Gamma} \mathcal{F}_\Gamma(R_2^0 u_0)\, d\Gamma \;=\; 0. \tag{6}$$

Neither the discrete divergence $\nabla_h \cdot$ nor the CENO approximation are defined by the definition of the reconstruction. Indeed, the reconstruction performed in each cell produces a global field which is generally discontinuous at cell interfaces $\partial C_i \cap \partial C_j$, see Fig.2. In order to fix an integration value at the interface, we can consider an arithmetic mean of the fluxes values for the two reconstruction values:

$$\mathcal{F}(R_2^0 u_0)^{quadrature}|_{\partial C_i \cap \partial C_j} \cdot \mathbf{n} = \frac{1}{2}\left(\mathcal{F}(R_2^0 u_0)|_{\partial C_i} + \mathcal{F}(R_2^0 u_0)|_{\partial C_j}\right) \cdot \mathbf{n} \tag{7}$$

where $(R_2^0 u_0)|_{\partial C_i}$ holds for the value at cell boundary of the reconstructed $R_2^0 u_0|_{C_i}$ on cell C_i. The above mean is applied on the four Gauss integration points $(\mathbf{g}_\alpha, \alpha = 1, 4)$ (two per interface segment, see Fig.4) necessary for an exact integration of quadratic polynomials. Then the accurate definition of B_h is as follows

$$\begin{aligned} &B_h(R_2^0 u_0, v_0) \;= \\ &\int_0^T \left\{ \sum_i \Big[\int_{C_i} v_0 \frac{\partial u_0}{\partial t} d\Omega + \int_{\partial C_i} v_0 \sum_{\alpha=0}^{\alpha=4} \frac{\mathcal{F}(R_2^0 u_0)|_{\partial C_i}(\mathbf{g}_\alpha) + \mathcal{F}(R_2^0 u_0)|_{\partial C_j}(\mathbf{g}_\alpha)}{8} d\sigma \Big] \right\} dt \\ &\qquad\qquad + \int_0^T \int_{\partial\Gamma} v_0 d\Gamma dt \end{aligned} \tag{8}$$

The discrete divergence involved in B is an extension of the continous one in the sense that when applied to a continuous function $\mathcal{F}$ these operators provide the same image ($\nabla \cdot \mathcal{F} = \nabla_h \cdot \mathcal{F}$). In particular, the restriction of B_h to smooth function is B and for the continuous solution u we have:

$$B_h(u, v_0) = B(u, v_0) = 0 \quad \forall\, v_0 \in \mathcal{C}^1([0, T]; \mathcal{V}_0). \tag{9}$$

It remains to define a time discretization for (6). We apply the standard explicit Runge-Kutta (RK4) time advancing. With the above central-diffferenced (7) spatial quadrature, this formulation

Prepared using fldauth.cls
DOI: 10.1002/fld

produces a central-differenced numerical approximation which is third-order accurate. However in a nonlinear setting, or on irregular unstructured meshes it cannot be used, due to a lack of stability.

3.3. Vertex-centered low dissipation CENO2

Scheme (6) is usually combined with an approximate Riemann solver instead of the formulation (7) proposed in the previous section. This latter option produces the usual upwind-CENO scheme, which is a rather dissipative third-order accurate scheme, enjoying a rather good nonlinear stability. Now, we are here interested only by advective effects, which are rather mildly non-linear effects. We keep the consistent central-differenced fluxes of scheme (6)-(7) but we add corrections of higher-order. Between two cell C_i and C_j we add to the central flux (7) two extra fluxes, which, in order to save computational costs, will be evaluated only on the mid-edge I of edge ik (Fig.2). These fluxes rely on higher-order derivatives of the unknown which we shall evaluate thanks to

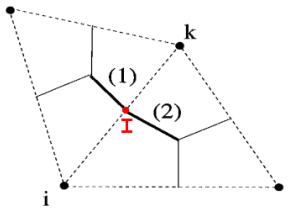

Figure 2. Sketch of the interface $\partial C_i \cap \partial C_k$ between cell C_i and cell C_k. It is made of two segments (1) and (2) between mid-edge I and triangles centroid.

the so-called "butterfly" molecule (Fig.3) built for every edge ik by identifying the "upwind" and "downwind" triangles crossed by edge $ik = [B_1 B_2]$. Here "upwind" and "downwind" refer only to edge direction. The other vertices are denoted C_1, D_1, C_2, D_2 according to the scheme in Fig.3. Points E_1 and E_2 are the intersection of edge $[B_1 B_2]$ with the opposite "upwind" and "downwind" triangle sides $[C_1 D_1]$ and $[C_2 D_2]$. Knowning the CENO-reconstructed Hessians on vertices allow their linear interpolation on points E_1 and E_2. Directional second-derivatives in direction $\overrightarrow{B_1 B_2}$ are then obtained at points E_1, B_1, E_2 and B_2. We then apply finite differences in order to get third and fourth directional derivatives at vertices B_1 and B_2. We denote by $u^{(2)}_{\overrightarrow{B_1 B_2}}(M)$, $u^{(3)}_{\overrightarrow{B_1 B_2}}(M)$ and $u^{(4)}_{\overrightarrow{B_1 B_2}}(M)$ the resulting approximate second, third, fourth directional derivatives along $\overrightarrow{B_1 B_2}$ at

Prepared using fldauth.cls
DOI: 10.1002/fld

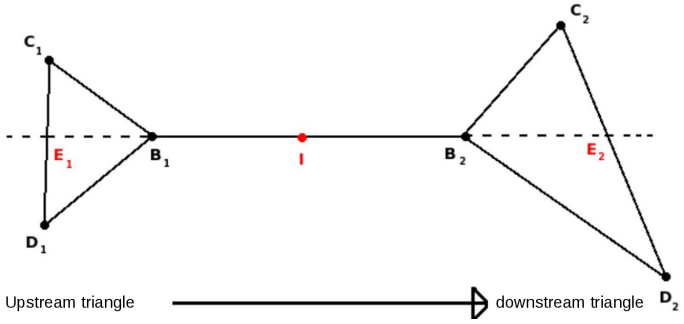

Figure 3. Butterfly molecule related to flux between cell around vertex B_1 and cell around vertex B_2. Vertices C_1, D_1, and C_2, D_2 are the other vertices of "upwind" and "downwind" triangles.

point $M \in [B_1B_2]$:

$$\begin{cases} u^{(3)}_{\overrightarrow{B_1B_2}}(B_1) = \dfrac{u^{(2)}_{\overrightarrow{B_1B_2}}(B_2) - u^{(2)}_{\overrightarrow{B_1B_2}}(E_1)}{2||\overrightarrow{B_1B_2}||} \\ u^{(3)}_{\overrightarrow{B_1B_2}}(B_2) = \dfrac{u^{(2)}_{\overrightarrow{B_1B_2}}(E_2) - u^{(2)}_{\overrightarrow{B_1B_2}}(B_1)}{2||\overrightarrow{B_1B_2}||} \\ u^{(4)}_{\overrightarrow{B_1B_2}}(B_1) = \dfrac{u^{(2)}_{\overrightarrow{B_1B_2}}(B_2) - 2u^{(2)}_{\overrightarrow{B_1B_2}}(B_1) + u^{(2)}_{\overrightarrow{B_1B_2}}(E_1)}{||\overrightarrow{B_1B_2}||^2} \\ u^{(4)}_{\overrightarrow{B_1B_2}}(B_2) = \dfrac{u^{(2)}_{\overrightarrow{B_1B_2}}(E_2) - 2u^{(2)}_{\overrightarrow{B_1B_2}}(B_2) + u^{(2)}_{\overrightarrow{B_1B_2}}(B_1)}{||\overrightarrow{B_1B_2}||^2} \end{cases}$$

The paradigm for improving the central-differenced CENO relies on an improved polynomial reconstruction $\mathbf{P}_i^{improved}$ of the unknown u in cells C_i and C_k to be applied for evaluating ik flux:

$$\begin{aligned} \mathbf{P}_i^{improved}(M) &= \mathbf{P}_i^{quadratic}(M) + \mathbf{P}_i^{(3)quadratic}(M) + \mathbf{P}_i^{(4)quadratic}(M) \\ \mathbf{P}_i^{(3)quadratic}(M) &= \left(-\frac{16}{5}\frac{1}{3!}\frac{||B_1M||^3}{2^3} u^{(3)}_{\overrightarrow{B_1B_2}}(i) \right) \\ \mathbf{P}_i^{(4)quadratic}(M) &= \left(\frac{1}{4!}\frac{||B_1M||^4}{2^4} u^{(4)}_{\overrightarrow{B_1B_2}}(i) \right). \end{aligned} \tag{10}$$

Prepared using fldauth.cls
DOI: 10.1002/fld

This reconstruction is injected in the flux between i and k according the following steps:

- The least-square quadratic reconstruction provides the polynomials $\mathbf{P}_i^2$ and $\mathbf{P}_k^2$ which will feed the third-order accurate ik-fluxes integrated without Riemann solver on the four Gauss points ($M = M_1, M_2, M_3, M_4$), see Fig.4.
- The two other terms of the improved reconstruction are evaluated simply on the mid-edge ($M = I$). A Roe-type upwinding with a Jacobian evaluated at mid-edge I is applied *solely* to these extra terms, see Fig.4.

When applying flux assembly to the two extra terms, two extra differentiations will result, namely, a first differentiation due to the difference in Roe diffusion term, and a second differentiation due to integral around each cell. This results in a dissipation term made of a sixth-order derivative and in an anti-dispersion term made of a fifth-order derivative. The dissipation term introduces much less damping than the one in upwind CENO2 (which involves a fourth order dissipation), and the anti-dispersion term compensates, in good part for unstructured meshes and totally for Cartesian meshes, the main term of dispersion of the original central-differenced CENO scheme. To illustrate

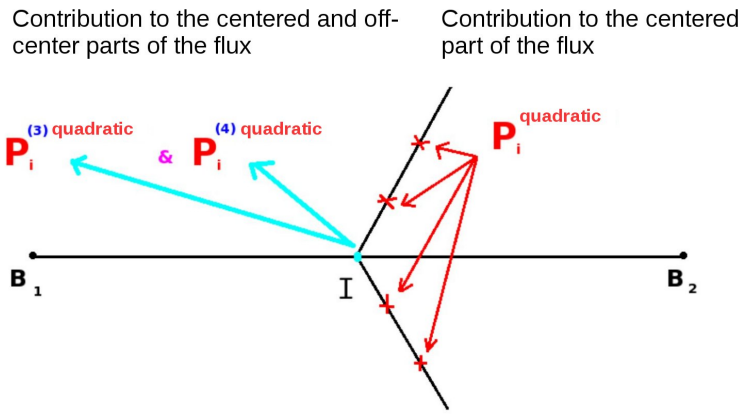

Figure 4. Quadrature of the presented CENO scheme between the two cells related to vertices B_1 and B_2: consistent CENO fluxes are evaluated on four Gauss points on interface, corrective antidispersive and dissipative fluxes are evaluated on the mid-edge point I.

the improvement which can be obtained, we computed the translation of a circular 2D Gaussian

Prepared using fldauth.cls
DOI: 10.1002/fld

discretised with 18 nodes along its diameter. The travel goes through 400 spatial intervals. With a RK4 time-advancing and a Courant number of 0.1, the *standard upwind* CENO scheme *i.e.* equipped with a Roe approximate solver applied to the consistent fluxes instead of the central formulation (7) results in a 28% damping. In contrast, the proposed improved CENO scheme gives a 25 times smaller maximal deviation (less than 1.12% damping) and a very low phase error, see Fig.5. The proposed correction only increases of 15% the total cost with respect to central differencing, but CENO reconstructions are rather computationally costly and the resulting scheme is 9-10 times slower than a usual second-order MUSCL scheme (in 2D). The reader interested by the improved scheme will find further details in [20].

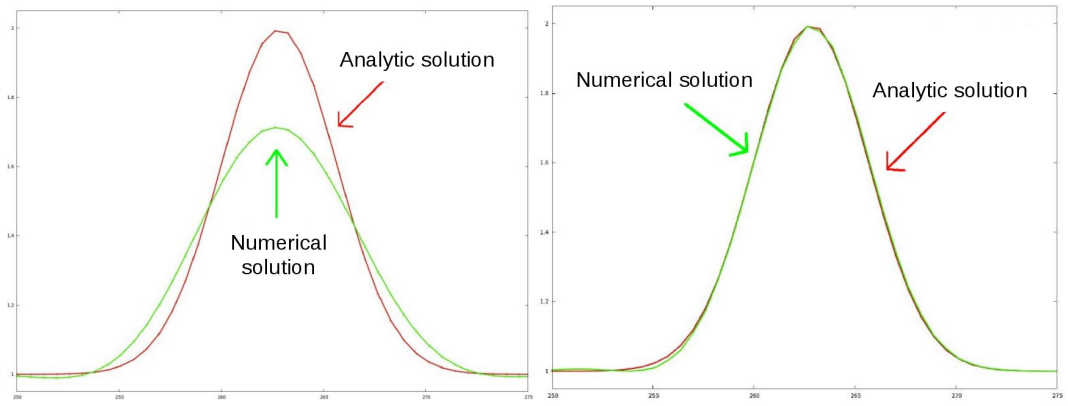

Figure 5. Improvement of the CENO scheme on the test case of a propagation of a 2D Gauss-shaped concentration. Left: comparison of the upwind third-order accurate CENO solution with the analytic solution. Right: comparison of the improved (third-order accurate) CENO scheme with the analytic solution.

4. ERROR ANALYSIS

In the present work, we do not consider time discretization errors. For explicit high-order time-advancing subject to a Courant-type condition, some argument for discarding the time-error analysis of advective models can be found in [3]. We then concentrate on spatial errors. Furthermore, we do not analyse the corrections terms introduced in Sec. 3.3. At least on regular meshes, these corrections terms are terms of higher order.

Prepared using fldauth.cls
DOI: 10.1002/fld

The proposed *a priori* analysis is in some manner the dual of the *a posteriori* analysis proposed by Barth and Larson in [7]. Let $j(u) = (g, u)$ be the scalar output which we want to accurately compute, where u is the solution of the continuous system (4). We concentrate on the reduction, by mesh adaptation, of the following error:

$$\delta j = (g, R_2^0 \pi_0 u - R_2^0 u_0)$$

where g is function of $L^2(\Omega)$ and u_0 the discrete solution of (6). The projection π_0 is defined by:

$$\pi_0 : \ v \mapsto \pi_0 v, \quad \pi_0 v|_{C_i} = \int_{C_i} v dx \quad \forall \, C_i, \text{dual cell.}$$

The adjoint state $u_0^* \in \mathcal{C}^1([0,T]; \mathcal{V}_0)$ is the solution of (B_h defined in (5)):

$$\frac{\partial B_h}{\partial u}(R_2^0 u_0)(R_2^0 v_0, u_0^*) = (g, R_2^0 v_0), \ \forall \, v_0 \in \mathcal{V}_0. \tag{11}$$

Then we can write, successively:

$$\begin{aligned} (g, R_2^0 \pi_0 u - R_2^0 u_0) &= \tfrac{\partial B_h}{\partial u}(R_2^0 u_0)(R_2^0 \pi_0 u - R_2^0 u_0, u_0^*) \quad \text{(adjoint eq.)(11)} \\ &\approx B_h(R_2^0 \pi_0 u, u_0^*) - B_h(R_2^0 u_0, u_0^*) \end{aligned}$$

and then

$$\begin{aligned} &(g, R_2^0 \pi_0 u - R_2^0 u_0) \\ &\approx B_h(R_2^0 \pi_0 u, u_0^*) \quad \text{(discrete state eq.)(5)(7)} \\ &\approx B_h(R_2^0 \pi_0 u, u_0^*) - B_h(u, u_0^*) \quad \text{(continuous state eq.)(4)(9)} \\ &\approx \tfrac{\partial B_h}{\partial u}(u)(R_2^0 \pi_0 u - u, u_0^*). \end{aligned}$$

For the case of Euler equations the previous error estimate writes:

$$\begin{aligned} \frac{\partial B_h}{\partial u}(u)(R_2^0 \pi_0 u - u, u_0^*) &= \\ \int_0^T \frac{\partial B_h^{time}}{\partial u}(u)(R_2^0 \pi_0 u - u, u_0^*) dt &+ \int_0^T \frac{\partial B_h^{Euler}}{\partial u}(u)(R_2^0 \pi_0 u - u, u_0^*) dt \end{aligned}$$

with

$$\begin{aligned} \frac{\partial B_h^{time}}{\partial u}(u)(R_2^0 \pi_0 u - u, u_0^*) &= \sum_i \int_{C_i} u_0^* (R_2^0 \pi_0 - Id) \frac{\partial u}{\partial t} dx \\ \frac{\partial B_h^{Euler}}{\partial u}(u)(R_2^0 \pi_0 u - u, u_0^*) &= \\ \sum_i \int_{C_i} u_0^* \nabla_h \cdot \mathcal{F}'(u)(R_2^0 \pi_0 u - u) dx &- \int_{\partial C_i \cap \Gamma} u_0^* \mathcal{F}'_\Gamma(u)(R_2^0 \pi_0 u - u) \, d\Gamma \end{aligned}$$

Prepared using fldauth.cls
DOI: 10.1002/fld

with the sum applied for all dual cell C_i of the mesh. Since, as in [43], *we do not consider the adaptation of boundary mesh*, we discard the boundary terms:

$$\frac{\partial B_h^{Euler}}{\partial u}(u)(R_2^0\pi_0 u - u, u_0^*) \approx \sum_i \sum_i \int_{C_i} u_0^* \nabla_h \cdot \mathcal{F}'(u)(R_2^0\pi_0 u - u) dx.$$

i.e:

$$\frac{\partial B_h^{Euler}}{\partial u}(u)(R_2^0\pi_0 u - u, u_0^*) - \int_{C_i} u_0^* \frac{\partial u_0}{\partial t} d\Omega \approx$$
$$\sum_{j\in\mathcal{V}(i)} \int_{\partial C_i \cap \partial C_j} u_0^* \sum_{\alpha=0}^{\alpha=4} \frac{\mathcal{F}'(u)(R_2^0\pi_0 u - u)|_{\partial C_i}(\mathbf{g}_\alpha) + \mathcal{F}'(u)(R_2^0\pi_0 u - u)|_{\partial C_j}(\mathbf{g}_\alpha)}{8} \cdot \mathbf{n} d\sigma \quad (12)$$

Let us examine the ingredients of the RHS integrand. First, u_0^* is constant by cell, with discontinuities at cell interface of amplitude of order of mesh size. The Jacobian $\mathcal{F}'(u)$ is smooth. The reconstruction error $R_2^0\pi_0 u - u$ is discontinuous at cell interfaces, but for a u smooth, the amplitude of this discontinuity is of order the third power of mesh size. Then:

$$\mathcal{F}'(u)(R_2^0\pi_0 u - u)|_{\partial C_k}(\mathbf{g}_\alpha) \approx \mathcal{F}'(u)(R_2^0\pi_0 u - u)(\mathbf{G}_i) \quad k = i \quad \text{or} \quad k = j \in \mathcal{V}(i).$$

where $\mathbf{G}_i$ is the centroid of cell C_i. Thus:

$$\frac{\partial B_h^{Euler}}{\partial u}(u)(R_2^0\pi_0 u - u, u_0^*) - \int_{C_i} u_0^* \frac{\partial u_0}{\partial t} d\Omega \approx$$
$$\mathcal{F}'(u)(R_2^0\pi_0 u - u)(\mathbf{G}_i) \cdot \sum_{j\in\mathcal{V}(i)} \int_{\partial C_i \cap \partial C_j} u_0^* \mathbf{n} d\sigma. \quad (13)$$

We recognize inside the RHS the approximation of a gradient of u_0^*:

$$\sum_{j\in\mathcal{V}(i)} \int_{\partial C_i \cap \partial C_j} u_0^* \mathbf{n} d\sigma \approx area(C_i) \boldsymbol{\nabla} u_0^*$$

thus:

$$\frac{\partial B_h^{Euler}}{\partial u}(u)(R_2^0\pi_0 u - u, u_0^*) - \int_{C_i} u_0^* \frac{\partial u_0}{\partial t} d\Omega \approx$$
$$area(C_i)\ \mathcal{F}'(u)(R_2^0\pi_0 u - u)(\mathbf{G}_i) \cdot \boldsymbol{\nabla} u_0^*.$$

As remarked in Sec.2, $R_2^0\pi_0 u - u$ can be replaced by a smooth function of the local third derivatives and local mesh size (factor $\frac{1}{3!}$ can be discarded in the rest of the analysis):

$$R_2^0\pi_0 u_q - u_q \preceq \sup_{\delta\mathbf{x}} |D^3 u(\mathbf{x})(\delta\mathbf{x})^3|, \quad \forall\ q = 1, 4.$$

Prepared using fldauth.cls
DOI: 10.1002/fld

For each flux component ($r = 1, 8$)

$$\mathcal{F}'_r(R_2^0\pi_0 u - u) \preceq \sup_{\delta\mathbf{x}} \sum_q ||\mathcal{F}'_{qr}||(D^3 u_q(\mathbf{x})(\delta\mathbf{x})^3).$$

Then:

$$|\delta j| \preceq \sum_q \int_\Omega K_q^{time}(u^*) \sup_{\delta\mathbf{x}} |D^3 \frac{\partial u}{\partial t}(\delta\mathbf{x})^3)| \, \mathrm{d}\Omega + 2 \sum_q \int_\Omega K_q^{Euler}(u, u^*) \sup_{\delta\mathbf{x}} |D^3 u(\delta\mathbf{x})^3)| \, \mathrm{d}\Omega$$

with

$$K_q^{time}(u^*) = |u^*| \quad ; \quad K_q^{Euler}(u, u^*) = \sum_r |(\mathcal{F}'_{rq}(u))^*| |\frac{\partial u_q^*}{\partial x_r}|$$

with the notation $\mathcal{F}$ according to (3), and

$$\partial u_q^*/\partial x_r = \partial u_q^*/\partial x \quad \text{for} \quad q = 1, 3, 5, 7,$$

$$\partial u_q^*/\partial x_r = \partial u_q^*/\partial y \quad \text{for} \quad q = 2, 4, 6, 8.$$

It will be useful to write it as follows:

$$|\delta j| \preceq \sup_{\delta\mathbf{x}} \mathbb{T}(|\delta\mathbf{x}|)^3$$

where $\mathbb{T}$ is the trilinear tensor:

$$\mathbb{T}(|\delta\mathbf{x}|)^3 = \sum_q \int_\Omega \left(K_q^{time}(u^*) |D^3 \frac{\partial u}{\partial t}| (|\delta\mathbf{x}|)^3 + K_q^{Euler}(u, u^*) |D^3 u| (|\delta\mathbf{x}|)^3 \right) \mathrm{d}\Omega. \tag{14}$$

Not surprisingly, the error is a third-order tensor in terms of the $\delta\mathbf{x}$, measuring local mesh size. In order to apply a metric-based mesh adaptation, we shall convert the estimate in a pseudo-quadratic estimate.

5. METRIC-BASED ERROR ESTIMATE

We consider the parametrization of the mesh by a Riemannian metric defined at each point $\mathbf{x} = (x, y)$ of the computational domain by providing at this point a symmetric matrix:

$$\mathcal{M}(\mathbf{x}) = d \, \mathcal{R}(\mathbf{x}) \Lambda(\mathbf{x}) \mathcal{R}^t(\mathbf{x}).$$

The rotation matrix $\mathcal{R} = (\mathbf{e}_\xi, \mathbf{e}_\eta)$, built with the normalised eigenvectors $\mathbf{e}_\xi = (e_\xi^x, e_\xi^y)$ and $\mathbf{e}_\eta = (e_\eta^x, e_\eta^y)$ of $\mathcal{M}$, parametrizes the two orthogonal stretching directions of the mesh. Denoting m_ξ

Prepared using fldauth.cls
DOI: 10.1002/fld

and m_η the two directional local mesh sizes in the characteristic/stretching directions of $\mathcal{M}$, the mesh density is $d = (m_\xi m_\eta)^{-1}$. Matrix Λ is a 2×2 diagonal one with eigenvalues $\lambda_1 = \frac{m_\xi}{m_\eta}$ and $\lambda_2 = \frac{m_\eta}{m_\xi}$ and of determinant equal to one. Any mesh which obeys reasonably to the mesh density and stretching specification of the metric is called a unit mesh of the metric (see for example [40]). In the case of a linear interpolation for a smooth (at least $\mathcal{C}^2$) solution u_q, the interpolation error is modelled by the following Hessian-based estimate (we discard the constant):

$$|u_q(\mathbf{x}) - \pi_1^{\mathcal{M}} u_q(\mathbf{x})| \;\approx\; |\frac{\partial^2 u_q}{\partial \tau_q^2}|(\delta\tau_q)^2 + |\frac{\partial^2 u_q}{\partial n_q^2}|(\delta n_q)^2 \;=\; \delta\mathbf{x}_{\mathcal{M}}|H_{u_q}|\delta\mathbf{x}_{\mathcal{M}}$$
$$= \; trace(\mathcal{M}^{-\frac{1}{2}}|H_{u_q}|\mathcal{M}^{-\frac{1}{2}}) \qquad (15)$$

where H_{u_q} is the Hessian of u_q, and orthonormal directions $\tau_q = (\tau_x^q, \tau_y^q)$ and $n_q = (n_x^q, n_y^q)$ are eigenvectors of this Hessian and $\delta\mathbf{x}_{\mathcal{M}}$ a vector of $\mathbb{R}^2$ such that $\delta\mathbf{x}_{\mathcal{M}}\mathcal{M}\delta\mathbf{x}_{\mathcal{M}} = 1$. This formulation permits the research of an optimal metric minimizing the linear interpolation error, [40].

In [46] the authors propose a general statement for an interpolation of arbitrary degree generalizing (15). We prefer here a simpler option. In order to address our third-order mesh adaptation problem in a similar manner to the Hessian-based approach, we propose instead to find from $\mathbb{T}$ a pseudo-Hessian $\tilde{H}_i$ on any vertex i in such a way that inside cell i we have:

$$\sup_{\delta\mathbf{x}} \mathbb{T}_i(|\delta\mathbf{x}|)^3 \approx \left(sup_{\delta\mathbf{x}}|\tilde{H}_i|(\delta\mathbf{x})^2\right)^{\frac{3}{2}} \quad \forall\delta\mathbf{x} \in \mathbb{R}^2.$$

In the continuous mesh model, the set of neighboring vertices j around a given vertex i is the surface of an ellipse centered on i and with small and large axis defined by the metric matrix $\mathcal{M}$. One way to adjust the pseudo-Hessian $\tilde{H}$ consistently with the discrete context is to minimize by least-squares the deviation between the quadratic term and the trilinear one on the neighbors of i in the current mesh:

$$\tilde{H}_i \;=\; Argmin \sum_{j=1}^{N(i)} \left(\tilde{H}_i(\vec{ij})^2 \;-\; (\mathbb{T}(\vec{ij})^3)^{2/3} \right)^2$$

with $\vec{ij} = (x_j - x_i, y_j - y_i) = (x_{ij}, y_{ij})$. Replacing then the trilinear estimate by the $3/2$ power of the quadratic term, we get:

$$\sup_{\delta\mathbf{x}} \mathbb{T}(|\delta\mathbf{x}|)^3 \preceq \left(trace(\mathcal{M}^{-\frac{1}{2}}|\tilde{H}_i|\mathcal{M}^{-\frac{1}{2}})\right)^{\frac{3}{2}} .$$

DOI: 10.1002/fld

We consider now a way to find a metric field which minimizes this error term.

6. OPTIMAL METRIC

Thanks to the above transformation of the error estimate, we can consider the minimization of the following error functional derived from estimate (14):

$$\mathcal{E}_0 \quad = \quad \sum_{q=1,4} \int_\Omega K_q(u,u^*) \left(trace(\mathcal{M}^{-\frac{1}{2}} |\tilde{H}_{u_q}| \mathcal{M}^{-\frac{1}{2}}) \right)^{\frac{3}{2}} \; dxdy.$$

We then obtain:

$$\mathcal{E}_0 \quad \preceq \quad \mathcal{E} = \int_\Omega \left(trace(\mathcal{M}^{-\frac{1}{2}} |S| \mathcal{M}^{-\frac{1}{2}}) \right)^{\frac{3}{2}} \; dxdy \quad \text{with} \quad S = \sum_{q=1,4} K_q(u,u^*)^{\frac{2}{3}} |\tilde{H}_{u_q}|. \tag{16}$$

Matrix $S(\mathbf{x})$ is a sum of symmetric positive definite matrices thus $S(\mathbf{x}) = \mathcal{R}_S(\mathbf{x}) \Lambda_S(\mathbf{x}) \mathcal{R}_S^t(\mathbf{x})$. We now identify the optimal metric, $\mathcal{M}^{opt} = \mathcal{M}^{opt}(N)$, among those having a prescribed total node number N, which minimizes the above error. We proceed similarly to the second-order metric analysis, e.g. [43] where optimal stretching directions are first derived and then optimal sizes are derived in a second step. To do so we re-write (16) as:

$$\int_\Omega \left(trace(\mathcal{M}^{-\frac{1}{2}} |S| \mathcal{M}^{-\frac{1}{2}}) \right)^{\frac{3}{2}} dxdy = \int_\Omega \left(trace(d_{\mathcal{M}}^{-1} (\mathcal{R}_{\mathcal{M}} \Lambda_{\mathcal{M}} \mathcal{R}_{\mathcal{M}}^T)^{-\frac{1}{2}} |S| (\mathcal{R}_{\mathcal{M}} \Lambda_{\mathcal{M}} \mathcal{R}_{\mathcal{M}}^T)^{-\frac{1}{2}}) \right)^{\frac{3}{2}} dxdy.$$

Mesh stretching direction. We first prescribe, at each point $\mathbf{x}$ of the computational domain Ω, the adapted metric eigenvectors *i.e.* the representation of the direction of stretching of mesh, $\mathcal{R}_{\mathcal{M}_{opt}}$ as aligned with the above error model, that is

$$\mathcal{R}_{\mathcal{M}_{opt}} = \mathcal{R}_{\mathcal{S}}.$$

Mesh stretching length. Let us minimize the error at each point $\mathbf{x}$ of the computational domain for a prescribed mesh density $d_{\mathcal{M}}$. We derive that the best ratio of eigenvalues for $\mathcal{M}$, *i.e.* the representation of mesh stretching or anisotropy should uniformize the two components of the error. This means that the product

$$(\mathcal{R}_{\mathcal{M}_{opt}} \Lambda_{\mathcal{M}_{opt}} \mathcal{R}_{\mathcal{M}_{opt}}^T)^{-\frac{1}{2}} |S| (\mathcal{R}_{\mathcal{M}_{opt}} \Lambda_{\mathcal{M}_{opt}} \mathcal{R}_{\mathcal{M}_{opt}}^T)^{-\frac{1}{2}}$$

Prepared using fldauth.cls
DOI: 10.1002/fld

is made proportional to identity. It implies that:

$$e_{opt} = \frac{(\lambda_{1_S})^{-\frac{1}{2}}}{(\lambda_{2_S})^{-\frac{1}{2}}} \quad ; \quad \Lambda_{\mathcal{M}_{opt}} = diag[e_{\mathcal{M}_{opt}}^{-1}, e_{\mathcal{M}_{opt}}]$$

in which we have enforced $det(\Lambda_{\mathcal{M}_{opt}}) = 1$. With these definitions of $\mathcal{R}_{\mathcal{M}_{opt}}$ and $\Lambda_{\mathcal{M}_{opt}}$, we get:

$$(\mathcal{R}_{\mathcal{M}_{opt}}\Lambda_{\mathcal{M}_{opt}}\mathcal{R}^T_{\mathcal{M}_{opt}})^{-\frac{1}{2}}|S|(\mathcal{R}_{\mathcal{M}_{opt}}\Lambda_{\mathcal{M}_{opt}}\mathcal{R}^T_{\mathcal{M}_{opt}})^{-\frac{1}{2}} = \begin{pmatrix} \lambda_{1_S}^{\frac{1}{2}}\lambda_{2_S}^{\frac{1}{2}} & 0 \\ 0 & \lambda_{1_S}^{\frac{1}{2}}\lambda_{2_S}^{\frac{1}{2}} \end{pmatrix}.$$

Inside this restricted family of metrics, it remains to define the optimal metric density. Let us consider the set of metrics with a total number of vertices prescribed to N:

$$\int_\Omega d\, dxdy = N. \tag{17}$$

We now have to minimise the L^1 norm of the error

$$\begin{aligned} \mathcal{E}(d) &= \int_\Omega d^{-\frac{3}{2}}\Gamma(S)\, dxdy \\ \Gamma(S) &= \left(trace\begin{pmatrix} \lambda_{1_S}^{\frac{1}{2}}\lambda_{2_S}^{\frac{1}{2}} & 0 \\ 0 & \lambda_{1_S}^{\frac{1}{2}}\lambda_{2_S}^{\frac{1}{2}} \end{pmatrix} \right)^{\frac{3}{2}} = (2\lambda_{1_S}^{\frac{1}{2}}\lambda_{2_S}^{\frac{1}{2}})^{\frac{3}{2}} \end{aligned} \tag{18}$$

with respect to d for a given number of nodes N. This means that:

$$\mathcal{E}'(d)\cdot\delta d = 0 \ \ \forall \ \ \delta d \ \text{ with } \int_\Omega \delta d\, dxdy = 0$$

which implies that the derivative $\Gamma(S)d^{-\frac{5}{2}}$ of integrand in $\mathcal{E}$ is constant and produces the optimal density:

$$d_{opt} = \frac{N}{C}_{opt}(\Gamma(S))^{\frac{2}{5}} = \frac{N}{C}_{opt}(2\lambda_{1_S}^{\frac{1}{2}}\lambda_{2_S}^{\frac{1}{2}})^{\frac{3}{5}} \quad \text{with} \quad C_{opt} = \int_\Omega (2\lambda_{1_S}^{\frac{1}{2}}\lambda_{2_S}^{\frac{1}{2}})^{\frac{3}{5}}\, dxdy.$$

This completes the definition of the optimal metric:

$$\mathcal{M}_{opt} = d_{opt}\mathcal{R}^t_{opt}\begin{pmatrix} e_{opt}^{-1} & 0 \\ 0 & e_{opt} \end{pmatrix}\mathcal{R}_{opt}.$$

Prepared using fldauth.cls
DOI: 10.1002/fld

7. FROM THEORY TO PRACTICAL APPLICATION

The previous analysis sets the optimal metric problem as the solution of the following continuous optimality conditions:

$$
\begin{aligned}
u \in \mathcal{V}\ ,\ \forall \varphi \in \mathcal{V}\ ,\ B(u,\varphi) = 0 \qquad & \text{“state system”} \\
u^* \in \mathcal{V}\ ,\ \forall \psi \in \mathcal{V}\ ,\ \Big(\frac{\partial B}{\partial u}\Big)(u,u^*)\psi = (g,\psi) \qquad & \text{“adjoint system”} \\
\mathcal{M}(\mathbf{x},t) = \mathcal{M}_{opt}(\mathbf{x},t) \qquad & \text{“control optimality”}.
\end{aligned}
$$

This system cannot be solved analytically and will be finally discretized. Not surprisingly, we choose the discrete state system as the one introduced previously. The adjoint is derived from its linearization. The last equation is discretized by recovering third-order derivatives by using a fourth-order reconstruction (like it would be done for a CENO3 scheme). Then, for each time step, the nonlinear iteration on the three equations of the optimality system provides an optimal metric and a unit mesh. In order to avoid to remesh too frequently we adopt the Global Transient Fixed Point algorithm introduced in [13]. The time interval has three embedded discretization: (1) time sub-intervals $]t_i, t_{i+1}[$ during which the mesh is frozen, (2) divisions $]t_{i,k}, t_{i,k+1}[$ of these sub-intervals for checkpointing state solution to be re-used backward in time for solving the adjoint system, (3) an even finer discretization in the time-steps $]t_{i,k} + m\delta t, t_{i,k} + (m+1)\delta t[$ used to advance in time. The algorithm is sketched in Fig.6 and writes:

```
 //--- Global Transient Fixed Point
For j=1,nptfx
 //--- Solve state once to get checkpoints
For i=1,nadap
```

- $\mathcal{S}^j_{0,i} = \texttt{ConservativeSolutionTransfer}(\mathcal{H}^j_{i-1}, \mathcal{S}^j_{i-1}, \mathcal{H}^j_i)$
- $\mathcal{S}^j_i = \texttt{SolveStateForward}(\mathcal{S}^j_{0,i}, \mathcal{H}^j_i)$

```
End for
```


Prepared using fldauth.cls
DOI: 10.1002/fld

```
    //--- Solve state forward and adjoint backward in time and
store samples
For i=nadap,1
```

- $(\mathcal{S}^*)_i^j = \texttt{AdjointStateTransfer}(\mathcal{H}_{i+1}^j, (\mathcal{S}_0^*)_{i+1}^j, \mathcal{H}_i^j)$
- $\{\mathcal{S}_i^j(k), (\mathcal{S}^*)_i^j(k)\}_{k=1,nk} = \texttt{SolveStateAndAdjointBackward}(\mathcal{S}_{0,i}^j, (\mathcal{S}^*)_i^j, \mathcal{H}_i^j)$
- $|\mathbf{H}_{\max}|_i^j = \texttt{ComputeGoalOrientedHessianMetric}(\mathcal{H}_i^j, \{\mathcal{S}_i^j(k), (\mathcal{S}^*)_i^j(k)\}_{k=1,nk})$

```
 End for
```

- $\mathcal{C}^j = \texttt{ComputeSpaceTimeComplexity}(\{|\mathbf{H}_{\max}|_i^j\}_{i=1,nadap})$
- $\{\mathcal{M}_i^{j-1}\}_{i=1,nadap} = \texttt{ComputeUnsteadyGoalOrientedMetrics}(\mathcal{C}^{j-1}, \{|\mathbf{H}_{\max}|_i^{j-1}\}_{i=1,nadap})$
- $\{\mathcal{H}_i^j\}_{i=1,nadap} = \texttt{GenerateAdaptedMeshes}(\{\mathcal{H}_i^{j-1}\}_{i=1,nadap}, \{\mathcal{M}_i^{j-1}\}_{i=1,nadap})$

```
End for
```

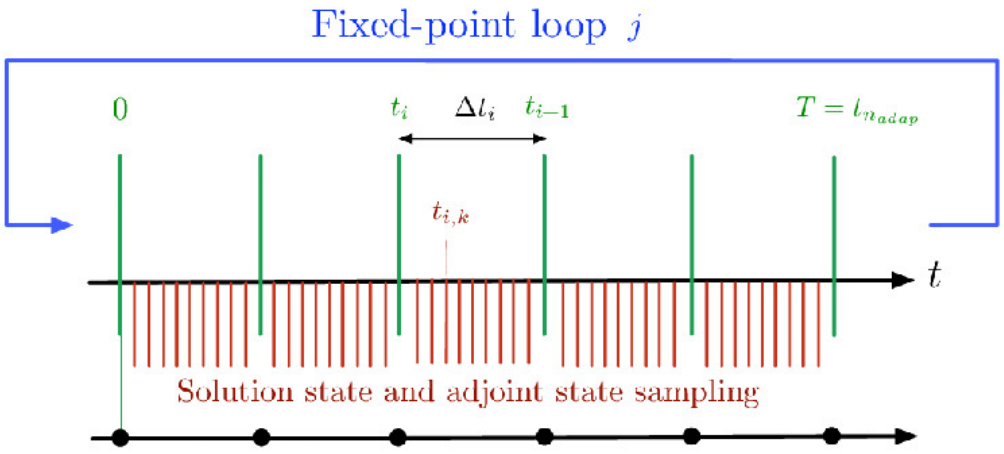

Figure 6. Global Transient Fixed Point for the goal-oriented "GO" adaptation of anisotropic meshes for an unsteady simulation.

A crucial criterion for evaluating a mesh adaptation method is its *a priori*/theoretical convergence order in terms of used degrees of freedom. Similarly, the evaluation of a computation should also rely on numerical convergence order, which should be preferably close to the theoretical one. An

DOI: 10.1002/fld

detailed discussion of the convergence of the global transient fixed point is presented in [13]. We recall now some useful features. The *space-time theoretical order* can be evaluated by considering space and time degrees of freedom. For an arbitrary flow (possibly with singularities) it is limited to $8/5$ (see [13]). The space-time numerical convergence needs to be measured by adequately decreasing mesh size, time-steps and increasing the number of mesh-adaptation intervals. In contrast, the *space theoretical order* is evaluated by considering solely spatial degrees of freedom. It should be as high as the theoretical spatial truncation order. It can be measured by solely increasing the mean number of vertices (for a fixed number of mesh-adaptation intervals).

8. TWO NUMERICAL TESTS

A goal-oriented mesh adaptation algorithm is not designed to deliver an accurate or even simply convergent solution field since the adaptation effort is restricted to the best accuracy for the scalar output. If the scalar output for a transient simulation is a time integral, an interesting accuracy evaluation of a mesh-adaptive calculation concerns the *integrand* of this time-integral. A successful mesh-adaptive calculation should show a third-order numerical convergence for a third-order accurate scheme. The two experiments which we present now both focus on the propagation of acoustic waves with an Euler model. It is a challenging simulation with a fixed but unstructured mesh for usual Euler schemes which are generally too dissipative and dispersive. It is also a challenging problem for mesh adaptation since meshes cannot be regular and must follow traveling structures which can go through the whole computational domain. We simulate the propagation of an acoustic wave between its emission and the time when the corresponding pressure fluctuation is recorded over a limited time interval with a microphone situated at some distance from the noise source. Not all sound waves will have influence on this record, and therefore, at each time level, only a part of the domain needs a fine mesh. And indeed, during these calculations, due to the effect of adjoint state, meshing concentrates only on a small part of the computational domain. We restrict to spatial acuracy and expect third-order convergence. In the two experiments which we describe, about 50

Prepared using fldauth.cls
DOI: 10.1002/fld

mesh-adaptation intervals (*i.e.* 50 meshes) are used in a time interval. The number of global fixed points iterations is 4. A typical wall time is 10 hours on a lap top for the finest mesh.

8.1. Noise propagation in a box

This experiment is rather close to the simulation computed in [13], for which the Global Transient Fixed Point algorithm was combined with a second-order accurate scheme. For a sequence of

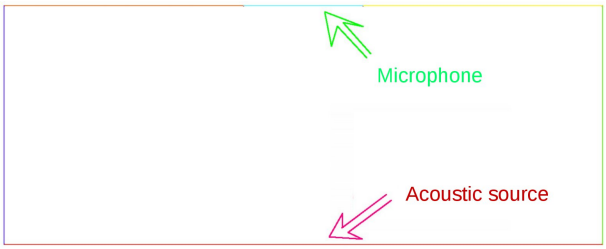

Figure 7. Propagation in a box: sketch of geometry. An acoustic source produces sound at the center of the bottom. The microphone integrates the pressure variation on a segment of the top wall.

adaptive meshes of 12K, 24K, 64K (mean size over the time interval), the numerical mesh convergence measured in [13] was 1.98. In the present work, a rectangular box (Fig.7) contains a source term with support restricted to a small half-disk on the middle of bottom side, and defined by $f = (0, 0, 0, r)$, where:

$$r = -A.exp\big(-B.ln(2)[x^2 + y^2]\big)C.cos(2\Pi fr)$$

with $A = 0.01$, $B = 256$, $C = 2.5$ and $f = 2$. The output functional is specified as:

$$j(W) = \int_0^T \int_M \frac{1}{2} k(t)\, \mathrm{d}M\mathrm{d}t = \int_0^T \int_M \frac{1}{2} (p(\mathbf{x}, t) - p_0)^2\, \mathrm{d}M\mathrm{d}t. \tag{19}$$

where p_0 is the initial pressure. The mesh and pressure contours of two mesh-adaptative transient computations, a coarse one and a fine one are presented in Fig. 8. The numerical convergence order of the functional is as expected close to third order. But the method seems to provide also some superconvergence for some outputs. Indeed, let us analyse the convergence of the time-integrand $k(t)$ of the functional:

$$k(t) = \int_M (p - p_0)\mathrm{d}M\,.$$

Prepared using fldauth.cls
DOI: 10.1002/fld

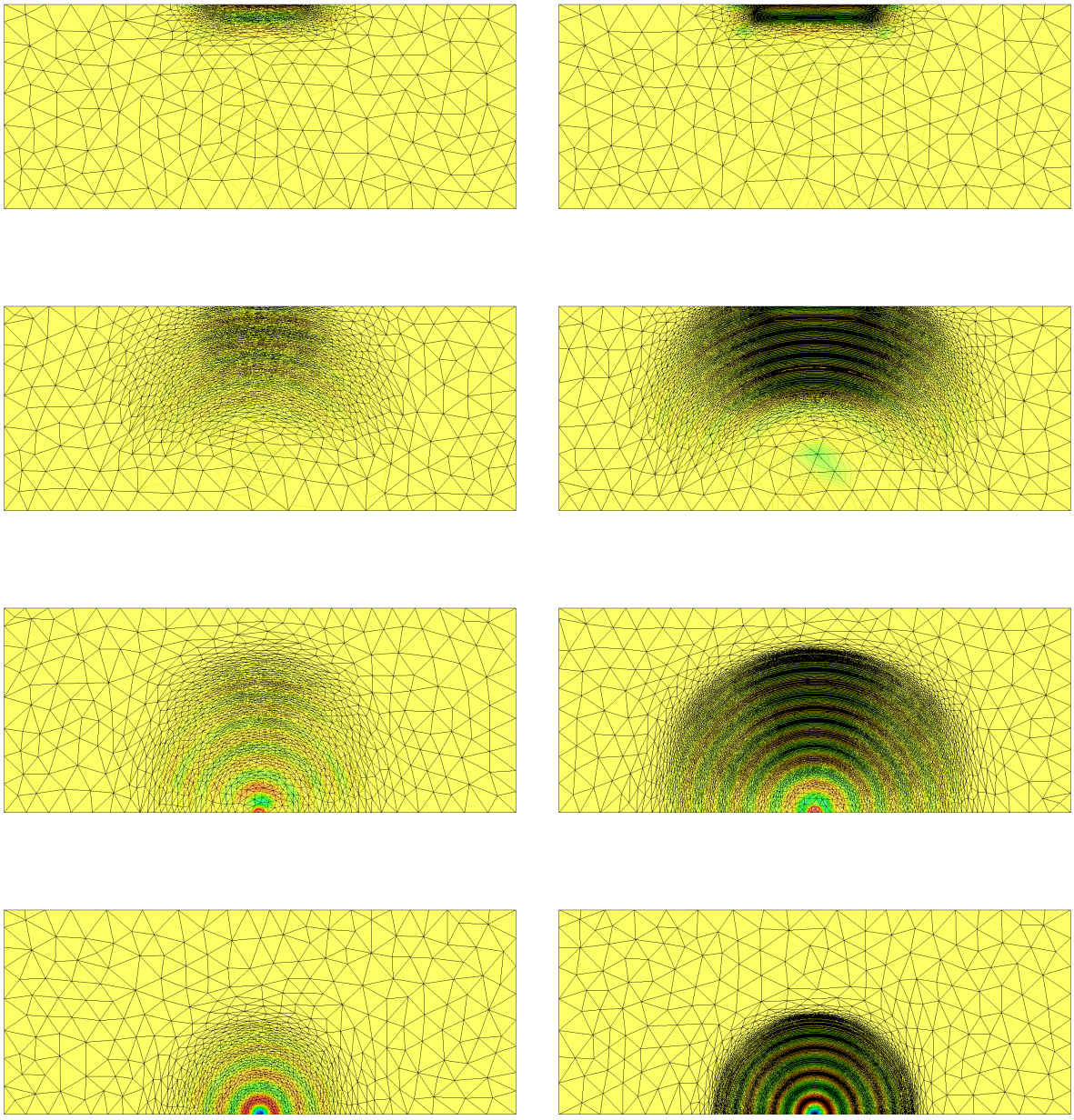

Figure 8. Acoustic waves traveling in a box from bottom (5th mesh in time) to top (20th mesh in time) with the coarse option (left, 1500 vertices in the mean) and the finest option (right, 21000 vertices in the mean).

at some particular time $t = t^*$ for the different mesh-adaptive calculations. The variations of k are depicted in Fig. 9. The numerical convergence for $k(t^*)$, is given by the usual relation

$$\frac{1 - \frac{N_2}{N_1}^{-\frac{\alpha}{d}}}{1 - \frac{N_3}{N_1}^{-\frac{\alpha}{d}}} \approx \frac{u_{N_1} - u_{N_2}}{u_{N_1} - u_{N_3}}$$

Prepared using fldauth.cls
DOI: 10.1002/fld

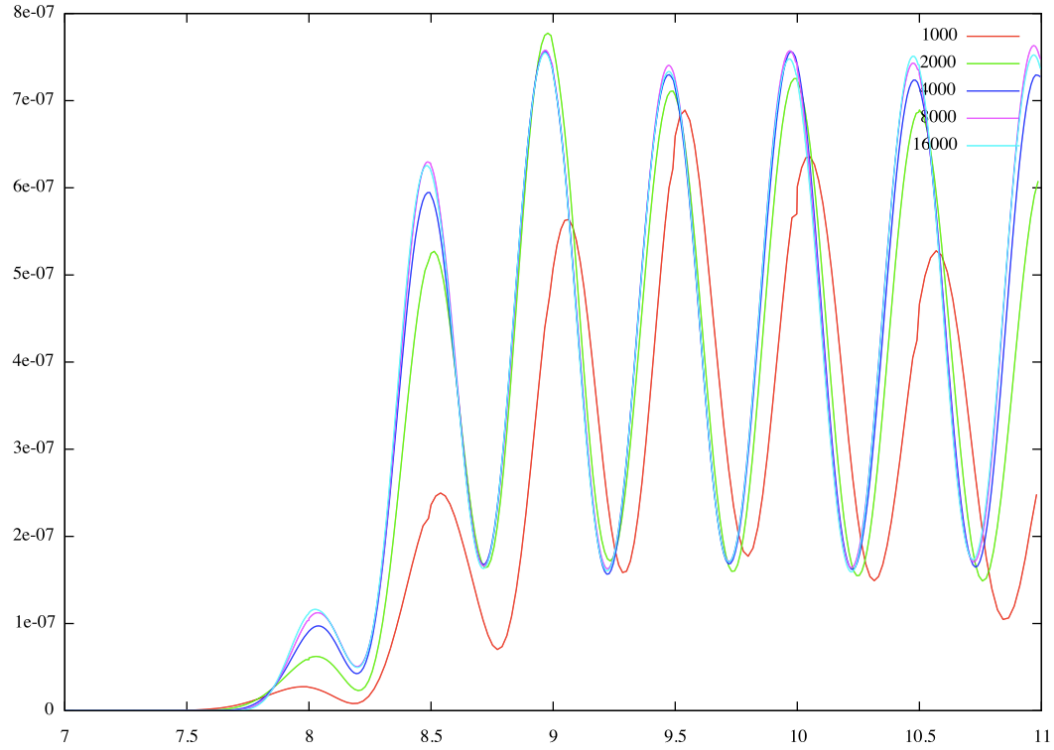

Figure 9. Noise propagation in a box: Mesh convergence of the spatial integral $k(t)$ (y-axis) as a function of time (x-axis). The lower curve "1000" corresponds to a mean mesh size of 1500 vertices. The three other curves, almost undistinguishable, correspond to mean mesh sizes of 5400, 11000, and 21000 vertices.

for three mesh sizes $N_1 < N_2 < N_3$ and N_3 and the corresponding solutions u_{N_1}, u_{N_2} and u_{N_3}. Numerical convergence order is measured on the maximum of k , reached for time close to $t^* = 10.5$. In our experiments, the mean mesh size is varied taking sucessively $1500, 5400, 11000, 21000$. For the three finer calculations, with mean mesh sizes of $5400, 11000, 21000$ vertices, convergence order appears as equal to 2.71, a level much higher than second order and close to the theoretical order 3 (cf. TabI). The meshes are anisotropic with aspect ratio larger than 3-4 in regions of interest. The smaller mesh size for the diffferent meshes (at different times) are of order of 5.10^{-4}, which would be obtained with a uniform isotropic mesh of about 2 million vertices.

8.2. Propagation/scattering on an anti-noise wall

The geometry is not a closed box. Only three components of the boundary are reflecting walls, namely (1) the ground, (2) an oblique wall, (3) a small rectangle, the "balcony", on the vertical right

Prepared using fldauth.cls
DOI: 10.1002/fld

Mean mesh size	Maximum close to T=10.5s	Observed convergence order
2775	$6.893079.10^{-07}$	
5403	$7.235717.10^{-07}$	
10696	$7.431403.10^{-07}$	**1.70**
21566	$7.510065.10^{-07}$	**2.71**

Table I. Noise propagation in a rectangular box: mesh convergence for the unsteady integrand.

side on which is put a micro (Fig.10). The oblique anti-noise wall should reduce the noise attaining the micro. We have the same source as (8.1) on the center of the bottom and the output scalar

Figure 10. Sketch of the anti-noise device: source at bottom, left, anti-noise wall in center of bottom region, balcony as part of left boundary.

functional is same as (19) but the spatial integral concerns an interval M on the vertical section of the balcony on right side (Fig. 10). The problem is more difficult than the previous one since a diffraction is computed around a non-smooth wall. The behavior of the time-dependent integrand is depicted in Fig.11 for two uniform-mesh calculations and four mesh adaptative calculations. The two uniform calculations use respectively 57791 and 117K vertices. They are poorly converging to the probable solution approximated by the fine mesh-adaptive calculations: convergence order

Prepared using fldauth.cls
DOI: 10.1002/fld

seems less than 1. Adapted meshes have respectively 2000, 7954, 15256, and 30980 vertices in the mean. Considering their most refined zones, where the mesh size is about 10^{-4} for the 30980 mesh, these adapted meshes should be roughly compared with uniform meshes of respectively 580K, 1.25M, 3.5M, and 5M vertices uniform meshes. For 2000 vertices, the convergence does not hold, but the approximation error is yet smaller than half of the uniform 117K error. This is coherent with our estimation of an equivalent uniform mesh of 580K. Over the triplet with 7954, 15256, and 30980, the results are close to each other (variation of 5%). We performed a numerical convergence analysis on the second maximum of k situated near $t = 13.$ in Tab.II. An idea of the fine meshes (mean size 30980) and density field is given in Figs.12,13,14,15,16. The meshes are anisotropic with an aspect ratio larger than 5 in the regions of interest. Numerical convergence order is 2.48, a figure less good than for the box calculation, but significantly higher than with a second-order-scheme.

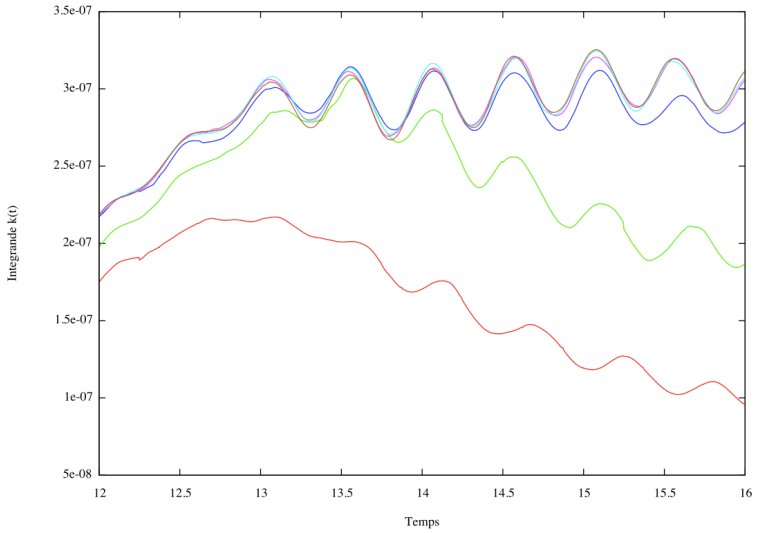

Figure 11. Anti-noise wall calculation. Time dependant integrand $k(t)$ of the functional for a series of two uniform meshes with respectively 57791 and $117K$ vertices (two lower curves) and a series of four mesh-adapted calculations with mean number of vertices 2000, 7954, 15256, and 30980. Convergence is observed for the three finest calculations.

Prepared using fldauth.cls
DOI: 10.1002/fld

Mean mesh size	**Second local maximum (i.e. near t=13)**	**Convergence order**
Adapted meshes (7954 vertices)	$3.119663e-07$	
Adapted meshes (15256 vertices)	$3.205026e-07$	
Adapted meshes (30980 vertices)	$3.245267e-07$	**2.48**

Table II. Mesh convergence order for the anti-noise wall calculation

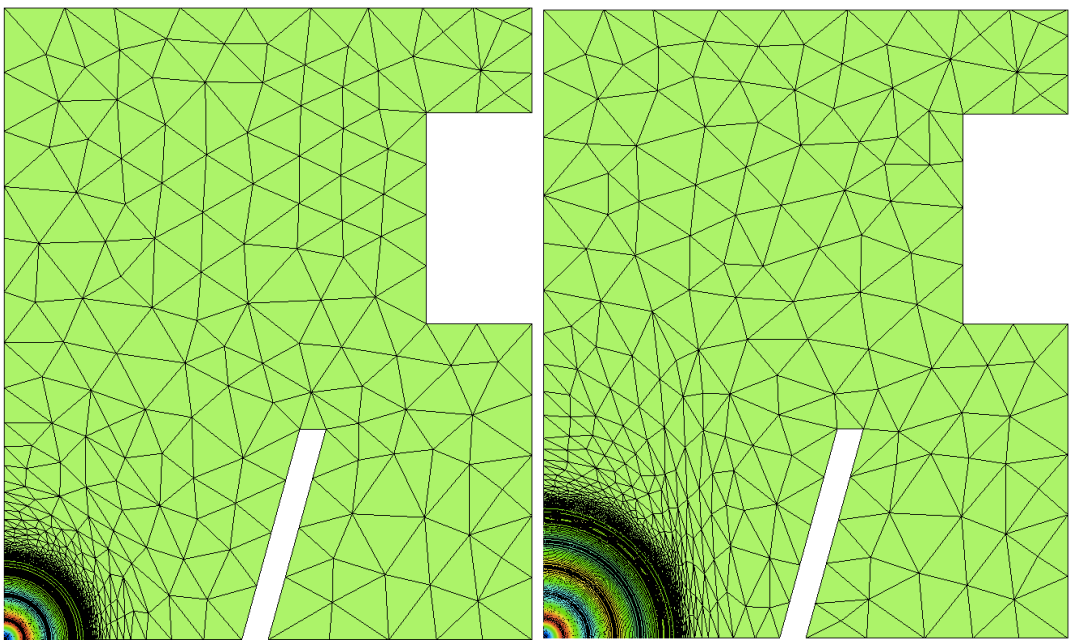

Figure 12. Anti-noise wall calculation for a mean of 30980 vertices. Density and mesh for first and fifth meshes used in time-interval 1 and 5.

Prepared using fldauth.cls
DOI: 10.1002/fld

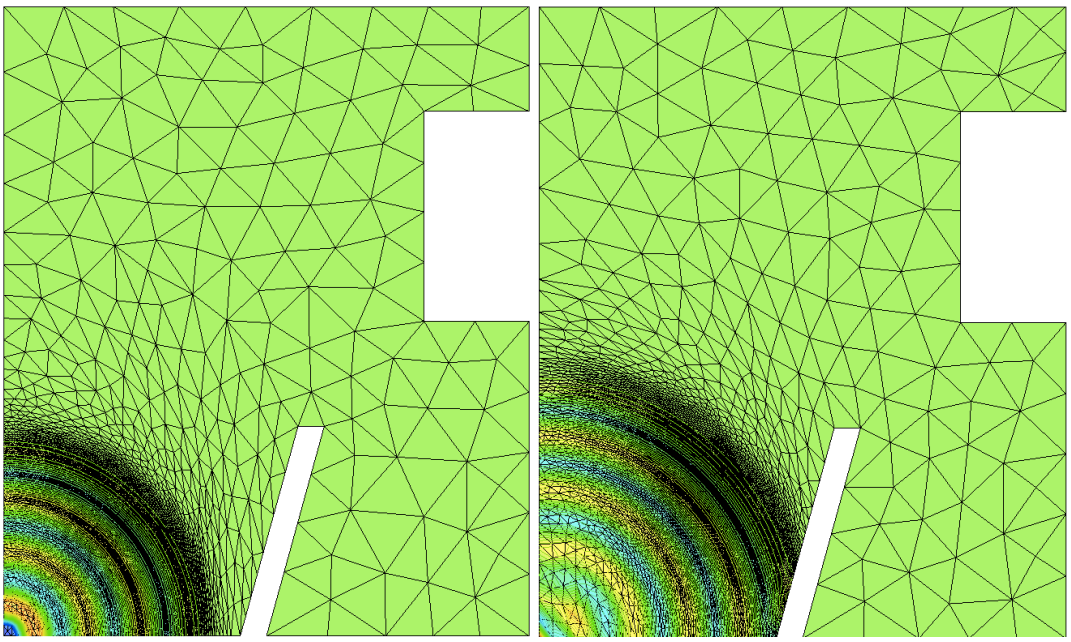

Figure 13. Anti-noise wall calculation for a mean of 30980 vertices. Density and mesh for first and fifth meshes used in time-interval 10 and 15.

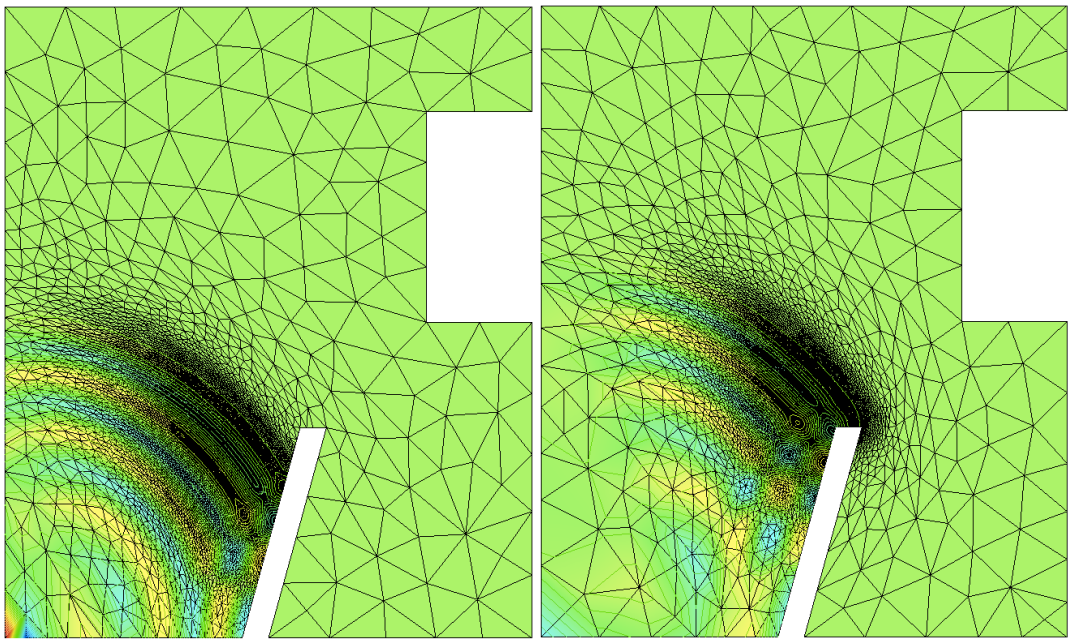

Figure 14. Anti-noise wall calculation for a mean of 30980 vertices. Density and mesh for first and fifth meshes used in time-interval 20 and 25.

Prepared using fldauth.cls
DOI: 10.1002/fld

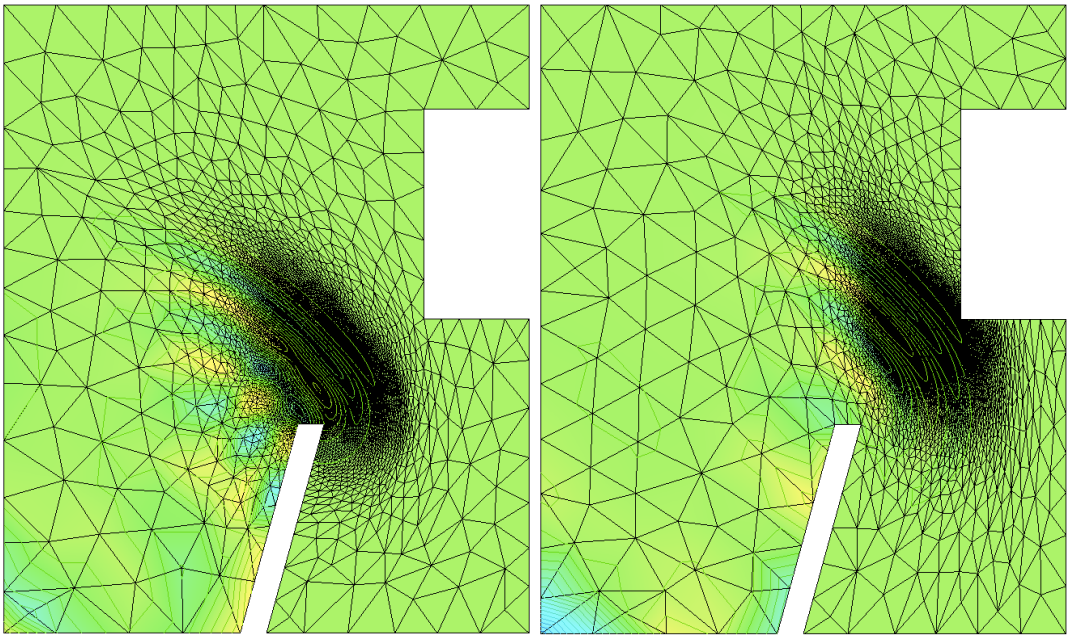

Figure 15. Anti-noise wall calculation for a mean of 30980 vertices. Density and mesh for first and fifth meshes used in time-interval 30 and 35.

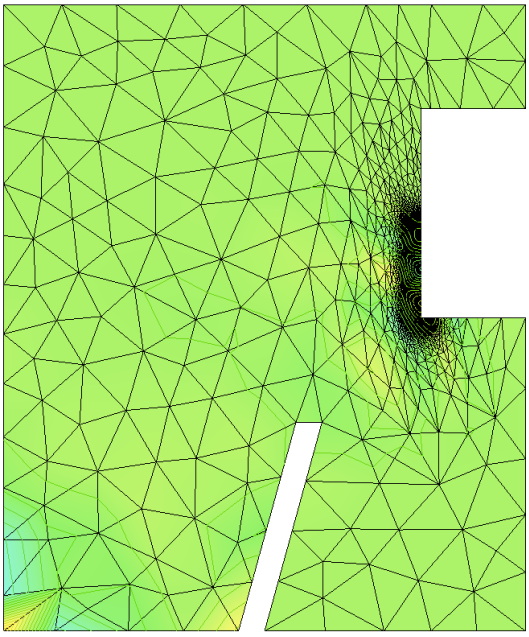

Figure 16. Anti-noise wall calculation for a mean of 30980 vertices. Density and mesh for first and fifth meshes used in time-interval 40 and 45.

Prepared using fldauth.cls
DOI: 10.1002/fld

9. CONCLUSION

In this exploratory study, we have proposed an a priori analysis of the error of a third-order accurate CENO scheme for the unsteady Euler equations. The proposed analysis expresses all distributed error terms as functions of reconstruction errors. It allows to predict the effect of a given mesh (mesh size, anisotropy) on the approximation error. An important simplification consists in projecting the estimate on a metric-based analysis thanks to Least-Squares. This allows for an anisotropic mesh adaptation relying on an optimal metric, and solving goal-oriented problematics. We complete the approach by considering a transient mesh adaptation loop. This loop is applied to two numerical examples focused on accurate advection of nonlinear acoustic waves with the Euler model. The numerical scheme effectively used is a version optimized for advection models. A convergence order between 2.48 and 2.71, much better than with second-order accurate adaptation, is obtained.

An important limitation observed in the results obtained with the proposed algorithm concerns the low maximum aspect ratio (4-5). Although obtaining high aspect ratios was not our primary purpose, this issue desserves, as remarked by our reviewers, argumented comments.

First we have to mention that before the present study, the first author developed in [19] a study in which, in place of a goal-oriented adaptation criterion, he used a sensor relying on the reconstruction error committed on the Mach number. In other terms, the third derivative of Mach number was used in the least square process to get what we called a pseudo-Hessian. The method was applied on a steady scram-jet test case in combination with TVD limiters adapted to the presented CENO scheme. We give two figures of this computation in Appendix. Then aspect ratios of at least 20 where obtained inside the numerical shocks. This shows that third derivatives normal to shock where evaluated as *large* by the process of derivation, and that the step of least square did not loose this information. But this does not necessarily show that the exact size of these derivative was well evaluated. By the way, acoustic test cases where also considered, then the obtained aspect ratios

Prepared using fldauth.cls
DOI: 10.1002/fld

where only about 2-5, lower than what the analytic sinusoidal behavior of the unsteady solution would let hope.

The state of our reflexion on this problem is that the combination of third-derivative evaluation with the present quasi-equilateral mesh generator is not sufficiently accurate. Now, the third derivative reconstruction relies on Least-Squares and use at least three layers of neighboring cells, which involve a suficiently large number of cells. We have observed that the output is rather sensitive to mesh regularity and orthogonality, when it is applied to a numerical solution obtained with the presented CENO approximation. It would probably be interesting to find a better reconstruction algorithm. Our option for future work is to use a newly derived mesh generator which enforces orthogonality properties, as in [44].

The method can be extended to 3D, but the central penalty of the proposed method is the high computational cost of our CENO third-order approximation scheme. This penalty would further amplify in 3D. Concerning the extension to viscous flow, the second-order accurate case has been addressed in a preliminary study, in [10], but even for second-order accuracy, many issues have to be addressed. For medium and high stretching, the use of a metric-orthogonal mesh generator as in [44] seems again compulsory. The next step of the extension of our analysis to third-order viscous models remains to be done. Again, this extension meets the issue of an efficient third-order approximation. Now, a third-order accurate CENO scheme seems to need a degree-three reconstruction for viscous fluxes. Then for futur study of third-order 3D mesh adaption, we will probably rely on a different numerical scheme. Indeed, the error analysis proposed in this work is based on the 2-exactness and can be rather easily adapted to other schemes enjoying 2-exactness (e.g. quadratic continuous and discontinuous Galerkin).

Goal-oriented formulation is not the only possible option and we mention that the estimates proposed in this paper also permits the extension of the mesh adaptation methodology to norm-oriented formulations, as in [15, 42].

Prepared using fldauth.cls
DOI: 10.1002/fld

10. ACKNOWLEDGEMENTS

This work has been supported by French National Research Agency (ANR) through projects ECINADS (ANR-09-COSI-003) and MAIDESC (ANR-13-MONU-0010). is work was granted access to the HPC resources of CINES under the allocations 2017-A0022A05067 and 2017-A0022A06386 made by GENCI (Grand Equipement National de Calcul Intensif).

11. APPENDIX: AN ADAPTATION BASED ON RECONSTRUCTION ERROR

In order to illustrate the discussion of our conclusion, we extract from [19] a calculation performed with the above CENO scheme combined with TVD limiters, and adapted according to the reconstruction error on a sensor, the Mach number (no adjoint is used). Iterative convergence between adaptation and computation is performed through a fixed point loop. The main differences with the computation presented in Section 8 are:

- the CFD problem is steady,

- solely the third derivative of Mach number is used for adaptation, in other words, the trilinear tensor of (14) is replaced by

$$\mathbb{T}_{Mach-reconstruction} = \int_{\Omega} |D^3 M|(|\delta \mathbf{x}|)^3 \, \mathrm{d}\Omega.$$

where M holds for the Mach number field.

We present in Fig.17 the Mach contour of an mesh adative calculation of a scramjet flow ($30,000$ vertices. The Fig.18 depicts a zoom of bottom leading edge showing the mesh stretching.

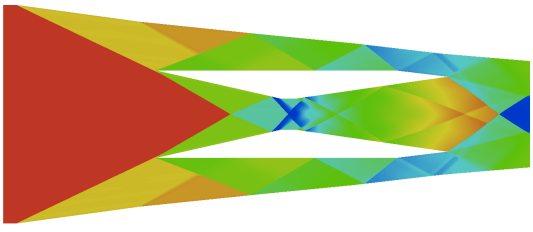

Figure 17. Mesh-adaptive calculation of a scramjet flow, Mach contours, global view.

Prepared using fldauth.cls
DOI: 10.1002/fld

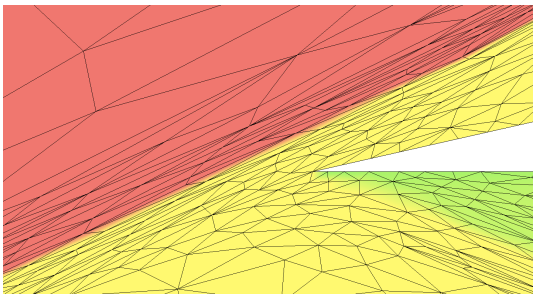

Figure 18. Mesh-adaptive calculation of a scramjet flow, Mach contours, zoom around the bottom leading edge (improved palette).

REFERENCES

1. R. Abgrall. Design of an essentially non-oscillatory reconstruction procedure on finite-element type meshes. *Rapport technique 1584, INRIA*, 1992.
2. R. Abgrall. Residual distribution schemes: current status and future trends. *Computers and Fluids*, 35:641–669, 2006.
3. F. Alauzet, P.J. Frey, P.L. George, and B. Mohammadi. 3D transient fixed point mesh adaptation for time-dependent problems: Application to CFD simulations. *J. Comp. Phys.*, 222:592–623, 2007.
4. T. Apel. *Anisotropic finite elements: Local estimates and applications*. Book Series: Advances in Numerical Mathematics. Teubner, Stuttgart, 1999.
5. T.J. Barth. Recent developments of high-order k-exact reconstruction on unstructured meshes. In *31st AIAA Aerospace Science Meeting*, AIAA-93-0668, Reno, NV, USA, 1993.
6. T.J. Barth and P.O. Frederickson. Higher order solution of the Euler equations on unstructured grids using quadratic reconstruction. *AIAA-90-0013*, 1990.
7. T.J. Barth and M.G. Larson. A-posteriori error estimation for higher order Godunov finite volume methods on unstructured meshes. In R. Herbin and D. Kröner, editors, *Finite Volumes for Complex Applications III*, pages 41–63, 2002.
8. F. Bassi and S. Rebay. High-order accurate discontinuous finite element solution of the 2D Euler equations. *J. Comp. Phys.*, 138(2):251–285, 1997.
9. Y. Belhamadia, A. Fortin, and E. Chamberland. Three-dimensional anisotropic mesh adaptation for phase change problems. *J. Comp. Phys.*, 201:753–770, 2004.
10. A. Belme. *Aérodynamique instationnaire et méthode adjointe*. PhD thesis, Université de Nice Sophia Antipolis, France, 2011.
11. A. Belme, F. Alauzet, and A. Dervieux. A priori anisotropic goal-oriented estimate and mesh adaptation for viscous compressible flow. *Preprint*, 2017.

Prepared using fldauth.cls
DOI: 10.1002/fld

12. A. Belme, A. Dervieux, and F. Alauzet. A fully anisotropic goal-oriented mesh adaptation for unsteady flows. In *Proceedings of the V ECCOMAS CFD Conf.*, 2010.
13. A. Belme, A. Dervieux, and F. Alauzet. Time accurate anisotropic goal-oriented mesh adaptation for unsteady flows. *J. Comp. Phys.*, 231(19):6323–6348, 2012.
14. C.L. Bottasso. Anisotropic mesh adaption by metric-driven optimization. *Int. J. Numer. Meth. Engng*, 60:597–639, 2004.
15. G. Brethes and A. Dervieux. Anisotropic norm-oriented mesh adaptation for a Poisson problem. *Journal of Computational Physics*, 322:804–826, 2016.
16. W. Cao. On the error of linear interpolation and the orientation, aspect ratio, and internal angles of a triangle. *SIAM J. Numer. Anal.*, 43(1):19–40, 2005.
17. W. Cao. An interpolation error estimate on anisotropic meshes in R^n and optimal metrics for mesh refinement. *SIAM J. Numer. Anal.*, 45(6):2368 2391, 2007.
18. W. Cao. An interpolation erreur estimate in R^2 based on the anisotropic measures of higher derivatives. *Math. Comp.*, 77:265–286, 2008.
19. A. Carabias. *Analyse et adaptation de maillage pour des schémas non-oscillatoires d'ordre élevé*. PhD thesis, Université de Nice-Sophia-Antipolis, France, 2013. (in French).
20. A. Carabias, O. Allain, and A. Dervieux. Dissipation and dispersion control of a quadratic-reconstruction advection scheme. In *European Workshop on High Order Nonlinear Numerical Methods for Evolutionary PDEs: Theory and Applications*, Trento, Italy, april 11-15, 2011.
21. M.R.J. Charest, C.P.T. Groth, and P.Q. Gauthier. A high-order central ENO finite-volume scheme for three-dimensional low-speed viscous flows on unstructured meshs. *Communications in Computational Physics*, 17(03):615–656, 2015.
22. P.G. Ciarlet and P.A. Raviart. General Lagrange and Hermite interpolation in R^n with applications to finite element methods. *Archive for Rational Mechanics and Analysis*, 46:177–199, 1972.
23. B. Cockburn. Devising Discontinuous Galerkin methods for non-linear hyperbolic conservation laws. *Journal of Computational and Applied Mathematics*, 128(1-2):187–204, 2001.
24. B. Cockburn, G. Karniadakis, and C.-W. Shu. *Discontinuous Galerkin methods: theory, computation and application*. Lecture Notes in Computational Science and Engineering. Springer Verlag, Berlin, 2000.
25. J. Dompierre, M.G. Vallet, M. Fortin, Y. Bourgault, and W.G. Habashi. Anisotropic mesh adaptation: towards a solver and user independent CFD. In *AIAA 35th Aerospace Sciences Meeting and Exhibit*, AIAA-1997-0861, Reno, NV, USA, Jan 1997.
26. S. Engquist, B. Harten, A. Osher, and S.R. Chakravarthy. Some results on uniformly high-order accurate essentially non oscillatory schemes. *Appl. Numer. Math. 2(3-5):347-377*, 1986.
27. A. Harten et S. Chakravarthy. Multi-dimensional ENO schemes for general geometries. *ICASE report 91-76*, 1991.
28. L. Formaggia, S. Micheletti, and S. Perotto. Anisotropic mesh adaptation in computational fluid dynamics: Application to the advection-diffusion-reaction and the Stokes problems. *Appl. Numer. Math.*, 51(4):511–533,

Prepared using fldauth.cls
DOI: 10.1002/fld

2004.

29. P.J. Frey and F. Alauzet. Anisotropic mesh adaptation for CFD computations. *Comput. Methods Appl. Mech. Engrg.*, 194(48-49):5068–5082, 2005.
30. C.P.T. Groth and L. Ivan. High-order solution-adaptive central essentially non-oscillatory (CENO) method for viscous flows. *49th AIAA Aerospace Sciences Meeting including the New Horizons Forum and Aerospace Exposition AIAA 2011-367 4 - 7 January 2011, Orlando, Florida*, 2011.
31. C. Gruau and T. Coupez. 3D tetrahedral, unstructured and anisotropic mesh generation with adaptation to natural and multidomain metric. *Comput. Methods Appl. Mech. Engrg.*, 194(48-49):4951–4976, 2005.
32. F. Hecht. Mesh generation and error indicator. *Summer School: more efficiency in finite element methods*, 2008.
33. F. Hecht and B. Mohammadi. Mesh adaptation by metric control for multi-scale phenomena and turbulence. In *35th AIAA Aerospace Sciences Meeting and Exhibit*, AIAA-1997-0859, Reno, NV, USA, Jan 1997.
34. W. Huang. Metric tensors for anisotropic mesh generation. *J. Comp. Phys.*, 204(2):633–665, 2005.
35. L. Ivan and C.P.T. Groth. High-order central ENO finite-volume scheme with adaptive mesh refinement. In *18th AIAA Computational Fluid Dynamics Conference*, AIAA-2007-4323, 25 - 28 June 2007, Miami, FL, 2007.
36. L. Ivan and C.P.T. Groth. High-order solution-adaptive central essentially non-oscillatory (CENO) method for viscous flows. *J. Comp. Phys.*, 257:830–862, 2014.
37. G. Kunert. *A Posteriori Error Estimation for Anisotropic Tetrahedral and Triangular Finite Element Meshes*. PhD thesis, Fakultatur Mathematik der Technischen Universita, Chemnitz, Germany, 1999.
38. F.C. Lafon and R. Abgrall. ENO schemes on unstructured meshes. *Rapport INRIA 2099*, Novembre 1993.
39. X. Li, M.S. Shephard, and M.W. Beal. 3D anisotropic mesh adaptation by mesh modification. *Comput. Methods Appl. Mech. Engrg.*, 194(48-49):4915–4950, 2005.
40. A. Loseille and F. Alauzet. Continuous mesh framework. Part I: well-posed continuous interpolation error. *SIAM Num. Anal.*, 49(1):38–60, 2011.
41. A. Loseille, A. Dervieux, and F. Alauzet. Fully anisotropic goal-oriented mesh adaptation for 3D steady Euler equations. *J. Comp. Phys.*, 229:2866–2897, 2010.
42. A. Loseille, A Dervieux, and F. Alauzet. Anisotropic norm-oriented mesh adaptation for compressible flows. In *53rd AIAA Aerospace Sciences Meeting, AIAA SciTech Forum, (AIAA 2015-2037)*, Kissimmee, Florida, Jan 5th, 2015.
43. A. Loseille, A. Dervieux, P.J. Frey, and F. Alauzet. Achievement of global second-order mesh convergence for discontinuous flows with adapted unstructured meshes. In *37th AIAA Fluid Dynamics Conference and Exhibit*, AIAA-2007-4186, Miami, FL, USA, Jun 2007.
44. A. Loseille, D.L. Marcum, and F. Alauzet. Alignment and orthogonality in anisotropic metric-based mesh adaptation. In *53rd AIAA Aerospace Sciences Meeting, AIAA SciTech Forum, (AIAA 2015-0915)*, Kissimmee, Florida, Jan 5th, 2015.
45. E. Mbinky. Adaptation de maillages pour des interpolations d'ordre très élevé. *Thèse de l'université Pierre et Marie Curie, Paris VI*, 2013.

Prepared using fldauth.cls
DOI: 10.1002/fld

46. E. Mbinky, F. Alauzet, and A. Loseille. High order interpolation for mesh adaptation. In *Proceedings of ECCOMAS CFD*, Vienna, Austria, 2012.

47. J-M. Mirebeau. Optimal meshes for finite elements of arbitrary order. *Springer Sciences + Business Media, LLC*, 2010.

48. H. Ouvrard, T. Kozubskaya, I. Abalakin, B. Koobus, and A. Dervieux. Advective vertex-centered reconstruction scheme on unstructured meshes. RR-7033, INRIA, 2009.

49. C.C. Pain, A.P. Humpleby, C.R.E. de Oliveira, and A.J.H. Goddard. Tetrahedral mesh optimisation and adaptivity for steady-state and transient finite element calculations. *Comput. Methods Appl. Mech. Engrg.*, 190:3771–3796, 2001.

50. C.W. Shu and B. Cockburn. Runge-Kutta Discontinuous Galerkin methods for convection-dominated problems. *J. Sci. Comput.*, 16(3):173–261, 2001.

51. A. Szymczak, A. Paszynska, M. Paszynski, and D. Pardo. Anisotropic 2D mesh adaptation in hp-adaptive FEM. *Procedia Computer Science*, 4:1818 1827, 2011.

52. A. Tam, D. Ait-Ali-Yahia, M.P. Robichaud, M. Moore, V. Kozel, and W.G. Habashi. Anisotropic mesh adaptation for 3D flows on structured and unstructured grids. *Comput. Methods Appl. Mech. Engrg.*, 189:1205–1230, 2000.

53. C.K.W. Tam and J.C. Webb. Dispersion-relation-preserving Finite Difference schemes for Computational Acoustics. *J. Comp. Phys.*, 107(2):262–281, 1993.

54. D.A. Venditti and D.L. Darmofal. Anisotropic grid adaptation for functional outputs: application to two-dimensional viscous flows. *J. Comp. Phys.*, 187(1):22–46, 2003.

Prepared using fldauth.cls
DOI: 10.1002/fld